Elimination of the reaction rate "scale effect": Application of the Lagrangian reactive particle-tracking method to simulate mixing-limited, field-scale biodegradation at the Schoolcraft (MI, USA) site.

Dong Ding[1], David A. Benson[1], Daniel Fernàndez-Garcia[2], Christopher V.

Henri[3], David W. Hyndman[4], Mantha S. Phanikumar[5], and Diogo Bolster[6]

———

[1]Hydrologic Science and Engineering,

Colorado School of Mines, Golden,

Colorado, 80401, USA

[2]Department of Geotechnical Engineering

and Geo-Sciences, Universitat Politecnica de

Catalunya, UPC-BarcelonaTech

[3]Center for Watershed Sciences,

University of California, Davis, CA, 95616,

USA

[4]Department of Earth and Environmental

Sciences, Michigan State University, East

Lansing, MI, USA

[5]Department of Civil and Environmental

Engineering, Michigan State University,

East Lansing, MI, USA

[6]Department of Civil and Environmental

Engineering and Earth Sciences, University

of Notre Dame, Notre Dame, Indiana, USA.

Abstract. Measured (or empirically fitted) reaction rates at groundwater remediation sites are typically much lower than those found in the same material at the batch- or laboratory-scale. The reduced rates are commonly attributed to poorer mixing at the larger scales. A variety of methods have been proposed to account for this scaling effect in reactive transport. In this study, we use the Lagrangian particle tracking and reaction (PTR) method to simulate a field bioremediation project at the Schoolcraft, Michigan site. A denitrifying bacterium, *Pseudomonas Stutzeri strain* KC (KC), was injected to the aquifer, along with sufficient substrate, to degrade the contaminant, Carbon Tetrachloride (CT), under anaerobic conditions. The PTR method simulates chemical reactions through probabilistic rules of particle collisions, interactions, and transformations to address the scale effect (lower apparent reaction rates for each level of upscaling, from batch- to column- to field-scale). In contrast to a prior Eulerian reaction model, the PTR method is able to match the field-scale experiment using the rate coefficients obtained from batch experiments.

1. Introduction

Bioremediation is an important technology to remove contaminant mass, especially organic pollutants, from aquifers. Application of an effective and efficient remediation system depends in large part on prediction of the time scale of contaminant degradation and/or removal. Thus, accurate characterization of the many reactive transport processes is critical in field-scale bioremediation design [*Steefel et al.*, 2005; *Hesse et al.*, 2009; *Scheibe et al.*, 2009].

Numerous modeling efforts have focused on developing mathematical equations to incorporate chemical reaction kinetics to the transport processes. The most common model is the advection-dispersion equation with the reaction as a source or sink term (ADRE) (e.g., [*Hesse et al.*, 2009; *Yabusaki et al.*, 2011; *Porta et al.*, 2012a; *Ding et al.*, 2013]). However, a variety of studies [*Chapelle and Lovley*, 1990; *Scholl*, 2000; *Phanikumar et al.*, 2005; *Meile and Tuncay*, 2006] indicated that the ADRE models using reaction parameters derived from laboratory experiments overestimated the field-scale reaction rates by orders-of-magnitude. One major reason is the "scale effect" for chemical reactions [*Lohse et al.*, 2009; *Rubin et al.*, 2012]; for instance, *Rubin et al.* [2012] suggested three possible scaling reasons that batch parameters may not be applicable to transport problems: 1) different timescales to reach chemical equilibrium; 2) different transfer rates due to the degree of mixing at different scales; and 3) different mass ratios of chemical saturation at different scales. Of these, poorer mixing of reactants induced by the increased heterogeneity of the transport media at larger scales may cause significantly reduced reaction rates [*Dentz et al.*, 2011; *Bolster et al.*, 2012].

Because parameters from laboratory-scale experiments have limited applicability to field-scale studies, effective reaction rates are usually used. The effective reaction rates vary from site to site and may change with time. The estimated parameters are also model dependent and are not directly related to any measurable property of the system [*Pedretti et al.*, 2013]. Because of the lack of model predictive ability, an accurate assessment of field-scale parameters would appear to require field-scale (in space and time) tests, obviating the advantage of model simulations.

The limited predictive capacity and uncertainty associated with the ADRE model in practice has prompted the development of other models to incorporate the effects of poor mixing. One of these is the Lagrangian particle tracking and reaction (PTR) algorithm, which simulates the reactive transport via Monte Carlo simulation of particle collision and interaction through probabilistic rules [*Waite*, 1957; *Gillespie*, 1976; *Benson and Meerschaert*, 2008; *Paster et al.*, 2014]. *Benson and Meerschaert* [2008] proposed a PTR method to simulate diffusion-controlled bimolecular reaction under incomplete mixing conditions. Their method showed that self-organized patterns of chemical heterogeneity engendered poor mixing and explained the slowed reaction at late times. The method was extended to moving flows, and the degree of mixing was linked to the number of particles used in a simulation, which represents the non-uniform distribution of initial concentrations (chemical heterogeneity) [*Paster et al.*, 2014]. The PTR method also successfully reproduced the results of two benchmark laboratory-scale column experiments that showed the "scale effect" of poor mixing relative to beaker-scale reactions [*Ding et al.*, 2013].

Moving toward the goal of simulating realistic field-scale experiments, *Ding and Benson* [2015] extended the PTR method to the Monod-type biodegradation and applied the method to a column experiment of Carbon Tetrachloride (CT) biodegradation. The authors found that various mechanisms that may contribute to slower biochemical reactions (e.g., crowding, enzyme de-activation) all manifest as diffusion-limited mixing. Therefore, the intricacies of bioremediation can be handeled by the PTR method. In this study, we focus on the application of the PTR method to accurately simulate reactive transport associated with bioremediation at the Schoolcraft site in Michigan, USA. Previous studies (e.g., [*Dybas et al.*, 2002; *Phanikumar et al.*, 2002, 2005]) noted the scale effect when moving from flask- to column- to field-scale biodegradation of CT. Our hypothesis is that a treatment of chemical heterogeneity by the PTR method will separate the poor-mixing effects from the previous empirical kinetic rate adjustments. In other words, we will test if the PTR method using bench-scale derived reaction rates is able to simulate the field-scale behavior.

2. Background

In the 1990s, a comprehensive field-scale bioremediation campaign was launched at the Schoolcraft site in Michigan (MI), USA [*Hyndman et al.*, 2000; *Phanikumar et al.*, 2005]. Numerous wells were installed, including many with continuous coring, to allow high-resolution measurements of hydraulic conductivities and chemical conditions. Cores were taken across the site to allow detailed characterization of aquifer properties. A line of wells (D1–D15) were installed in a manner that allowed injection and/or withdrawal of biologic agents and nutrients for implementation of bioremediation (Figure 1c). Finally, a series of multi-level wells was installed to monitor the progress of the remediation experiment.

2.1. The basis of bioremediation: Laboratory work

Prior to conducting the field-scale bioremediation at the site, laboratory studies [*Dybas et al.*, 1995; *Mayotte et al.*, 1996] revealed that a denitrifying bacterium, *Pseudomonas Stutzeri strain* KC (KC), in the presence of sufficient substrate, can rapidly degrade CT to carbon dioxide, formate, and dechlorinated non-volatile byproducts under anaerobic conditions without producing chloroform, a more persistent contaminant. With this finding, biodegradation of CT by KC was tested in the laboratory and field. Tests included batch (flask) experiments [*Criddle et al.*, 1990; *Dybas et al.*, 1995], column experiments [*Witt et al.*, 1999; *Phanikumar et al.*, 2002], and pilot studies [*Dybas et al.*, 1998]. One level of upscaling was achieved in the laboratory when a no-flow column experiment was conducted by *Witt et al.* [1999]. In this experiment, a 100 cm-long column was filled with sediments and groundwater extracted from site borings. The groundwater was supplemented with initial concentrations of CT and nitrate at 0.1 and 25 milligrams per liter (mg/L), respectively. The column was inoculated with KC, acetate, and base (to mediate the pH) at the center of the column (between 44.4 and 59.6 cm) and was maintained as a static incubation. The inoculation had KC at $1.2 \pm 0.1 \times 10^8$ colony-forming units per milliliter (CFU/mL) and an acetate concentration of $1,533$ mg/L. One CFU/mL is approximately equal to 1.67×10^{-7} ppm for strain KC [*Phanikumar et al.*, 2002]. The column had 10 sampling ports spaced at 7.6-cm intervals to monitor the concentrations of dissolved species and biomass. Over the course of a month, a significant fraction of CT was degraded, demonstrating the viability of the technology.

2.2. Site Information

107   The unconfined aquifer at the Schoolcraft site is composed of glaciofluvial sediments

108   overlying a thick clay unit, which acts as an aquitard [*Kehew et al.*, 1996; *Phanikumar*

109   *et al.*, 2005]. The top of the aquitard was found at approximately 27.3 meters (m) below

110   ground surface (bgs), while the water table was around 4.5 m bgs [*Hyndman et al.*, 2000].

111   The natural hydraulic gradient at the site was roughly 0.001, with a general groundwater

112   flow direction from northwest to southeast (Figure 1).

113   As part of the installation of the bioremediation delivery and monitoring wells, 346 soil

114   core samples were taken from 11 borings, repacked and placed in constant-head perme-

115   ameters. The repacked samples were shown to be reasonable estimates of the horizontal

116   hydraulic conductivity (K) values according to a model verification of tracer tests against

117   observed concentration profiles [*Biteman et al.*, 2004]. The K analysis and core logging re-

118   vealed 4 stratigraphic zones, with mean $\ln(K)$ (cm/s) of -1.26, -1.81, -1.49, and -1.86,

119   from deepest to shallowest. In general, the highest K zone exists at the bottom of the

120   aquifer. The large number of samples allowed an estimate of the anisotropic variograms

121   in each zone. In general, the variogram ranges in the horizontal directions were estimated

122   to be from 3 to 18 m, and vertical ranges were from 0.35 to 1.62 m. The overall variance

123   of $\ln(K)$ is 0.634. Flow and bromide tracer transport modeling (discussed in more detail

124   below) showed that the K-field generated from zonal kriging was superior to non-zonal

125   kriging [*Biteman et al.*, 2004]. We will use this K field (Figure 2), as did *Phanikumar et al.*

126   [2005], to simulate flow conditions during the bromide tracer test and the bioremediation

127   experiment.

128   There were several contaminant plumes reported in the aquifer [*Hyndman et al.*, 2000;

129   *Dybas et al.*, 2002]. The field remediation experiment was conducted within a plume,

130 designated Plume A, which was contaminated with carbon tetrachloride (CT) [*Hyndman*

131 *et al.*, 2000; *Phanikumar et al.*, 2005]. The CT contamination within plume A was 1, 600

132 m long and 160 m wide [*Phanikumar et al.*, 2005]. Concentrations from 221 locations

133 indicated that higher CT concentrations were in the deeper, high-conductivity part of the

134 aquifer, as illustrated in Figure 3.

2.3. Bioremediation Method

135 The field remediation system at the Schoolcraft site was designed to inoculate non-native

136 microbes and recirculate the groundwater through pumping from a series of wells aligned

137 perpendicular to the natural gradient flow (Figure 1). These pumping wells were screened

138 from 9.1 to 24.4 m bgs using 0.025 cm slotted screen [*Hyndman et al.*, 2000]. A total of

139 134 piezometers, each with 0.33 m-long screens across the vertical extent of the plume,

140 composed the monitoring array to record the concentrations. Prior to the bioremediation,

141 a bromide tracer test was conducted under the approximate cyclic injection/withdrawal

142 cycle for 20 days to assess transport rates within the contaminated heterogeneous aquifer

143 unit [*Phanikumar et al.*, 2005].

144 To initiate the bioremediation process, a single inoculation was conducted using 18, 900

145 L of KC-laden groundwater through the fifteen (15) delivery wells, which were 1 m apart.

146 The locations of these wells (names start with D) are shown in Figure 1. Groundwater

147 was recirculated for 6 hours every week through pumping and injection. The recirculation

148 consisted of: 1) extracting from every other well (e.g., even numbered wells: D02, D04,

149 . . . , D14) and re-injecting into intervening wells (e.g., odd numbered wells: D01, D03, . . . ,

150 D15) after addition of constituents (acetate, bromide, pH amendment, etc.) for 5 hours;

151 2) reversing the pumping/injection (e.g., pumping from odd numbered wells and injecting

¹⁵² back to the even numbered wells) for 1 hour; and 3) keeping natural flow condition for

¹⁵³ the rest of the week. The pumping/injecting orders (even or odd numbered) on wells in

¹⁵⁴ the first two stages were switched in the following weeks. The details are described by

¹⁵⁵ *Phanikumar et al.* [2005]. The circulation and monitoring were conducted for 165 days.

3. Methods and Models

3.1. The Simple Form of Enzymatic Reaction

¹⁵⁶ Biodegradation occurs as microorganisms metabolize accessible nutrients (substrates)

¹⁵⁷ to grow. The substrates, including organic contaminants, are degraded to inorganics or

¹⁵⁸ smaller molecules by biomass [*Alexander*, 1999; *King et al.*, 2010]. A simple biodegrada-

¹⁵⁹ tion (1) following this mechanism under certain conditions can be characterized by the

¹⁶⁰ Monod equation [*Monod*, 1949].

$$S + E \underset{k_r}{\overset{k_f}{\rightleftharpoons}} ES \xrightarrow{k_c} E + \mathrm{P}, \tag{1}$$

¹⁶¹ where k_f, k_r, and k_c are forward, reverse and conversion (transform) rate constants.

¹⁶² The substrate S and the biomass or enzyme E form the intermediate enzyme/substrate

¹⁶³ complex ES through the initial bimolecular reaction with a rate constant k_f [M^{-1}T^{-1}].

¹⁶⁴ The ES complex can dissociate to E and S, with a rate constant k_r [T^{-1}], or proceed to

¹⁶⁵ form the product P, with a rate constant k_c [T^{-1}].

166 Under perfectly-mixed conditions, the rates of concentration change are quantified

167 through the law of mass action:

$$d[S]/dt = -k_f[E][S] + k_r[ES] \tag{2a}$$

$$d[E]/dt = -k_f[E][S] + k_r[ES] + k_c[ES] \tag{2b}$$

$$d[ES]/dt = k_f[E][S] - k_r[ES] - k_c[ES] \tag{2c}$$

$$d[P]/dt = k_c[ES] \tag{2d}$$

168 *Michaelis and Menten* [1913] originally proposed a simple solution of (3) by assuming

169 that 1) only a vanishingly small fraction of substrate is bound by enzyme, 2) the complex

170 is very labile and decays to free enzyme, 3) the substrate is in instantaneous chemical

171 equilibrium with the complex, and 4) the conversion rate is directly proportional to the

172 concentration of enzyme. Under these conditions, Eqs. (2) reduce to

$$\frac{d[P]}{dt} = v_{max}\frac{[S]}{K_S + [S]} = k_c[E]_0\frac{[S]}{K_S + [S]}, \tag{3}$$

173 where the conversion rate $v_{max} \equiv k_c[E]_0$ and $[E]_0$ is the initial enzyme concentration, and

174 K_S is the half saturation coefficient, or Michaelis constant, defined by $(k_r + k_c)/k_f$.

3.2. ADRE-based Model

175 Employing the Monod/Michaelis-Menten (hereafter called M-M) kinetics, *Phanikumar*

176 *et al.* [2005] developed a reactive transport model (Eqs. 4) specifically for CT bioremedi-

177 ation to account for microbial-mediated reactions, advection, dispersion, attachment, and

178 detachment of reactants:

$$\frac{\partial E}{\partial t} = \mathcal{L}_E(E) + \left[\mu_{max} \frac{S}{K_S + S} \frac{A}{K_A + A} - k_{decay} \left(1 - \frac{A}{K_A + A} \right) - k_{att} \right] E$$
$$+ k_{det} \left(1 - \frac{A}{K_A + A} \right) X + Q^s E^s \tag{4a}$$

$$\frac{\partial X}{\partial t} = \left[\mu_{max} \frac{S}{K_S + S} \frac{A}{K_A + A} - (k_{decay} + k_{det}) \left(1 - \frac{A}{K_A + A} \right) \right] X + k_{att} E \tag{4b}$$

$$\frac{\partial S}{\partial t} = \mathcal{L}_S(S) - \left(\frac{\mu_{max}}{Y_n} \frac{S}{K_S + S} \frac{A}{K_A + A} + \gamma \frac{S}{K_S + S} \right) (E + X) -$$
$$\frac{k_{decay}}{Y_{nd}} \left(1 - \frac{A}{K_A + A} \right) (E + X) + Q^s S^s \tag{4c}$$

$$\frac{\partial A}{\partial t} = \mathcal{L}_A(A) - \frac{\mu_{max}}{Y_a} \frac{S}{K_S + S} \frac{A}{K_A + A} (E + X) + Q^s A^s \tag{4d}$$

$$\left(1 + \frac{\rho f K_d}{\theta} \right) \frac{\partial c}{\partial t} = \mathcal{L}_c(c) - k' c \left(E + X \frac{\rho f K_d}{\theta} \right)$$
$$- \frac{\rho k_{des} c}{\theta} [(1 - f) K_d c - c_S] + Q^s c^s \tag{4e}$$

$$\frac{\partial c_S}{\partial t} = k_{des} [(1 - f) c K_d - c_S] - k' c_S X \tag{4f}$$

where we dropped the square brackets when denoting concentration, E is the concentration of mobile bacteria; X is the amount of bacteria attached to solids; S is the substrate, nitrate; A is the concentration of acetate; c is the concentration of CT, and c_S is the concentration of CT adsorbed to the solids. The concentrations have units of mg/L, including the mobile and immobile bacteria, which have the units converted from CFU/mL [*Phanikumar et al.*, 2005]. For each mobile species, there is a linear advection/dispersion operator $\mathcal{L}(f) = -\nabla \cdot (\boldsymbol{v} f - \boldsymbol{D} \nabla f)$ that includes the effects of spatio-temporally variable velocity $\boldsymbol{v}$ and species-dependent diffusion/dispersion tensor $\boldsymbol{D}$. Q^s is the flow of source/sink term, and the s superscript denotes the concentration of each constituent in the source/sink term. K_S and K_A are half saturation constants for nitrate and acetate, respectively, μ_{max} is the maximum conversion rate, k_{decay} is biomass decay rate, k_{att} is the attachment coefficient of biomass, k_{det} is the detachment coefficient of biomass, k' is the

191 degradation rate for CT, and k_{des} is the desorption rate of CT. Y_n, Y_a, and Y_{nd} are the

192 cell yields for nitrate, acetate, and biomass consuming nitrate, respectively. The factor f

193 is the fraction of exchange sites at equilibrium, K_d is the CT distribution coefficient, ρ is

194 the bulk density of soil, and γ is the nitrate utilization rate by indigenous microflora or

195 endogenous respiration. The population of indigenous microflora is assumed proportional

196 to the KC bacteria and its reactions have the same form as those of KC [*Phanikumar*

197 *et al.*, 2002].

198 In this model, a correction factor $[1 - A/(K_A + A)]$ was added to the bacteria decay

199 term to account for the increase of decay rate at low nutrient concentration [*Beeftink et al.*,

200 1990; *Phanikumar et al.*, 2005]. However, recent models (i.e., [*Tan et al.*, 1994; *Tufenkji*,

201 2007; *Ding*, 2010]) assumed that the decay rate is independent of the concentration of

202 nutrient. Thus, we moderately modified the models as Eqs. 5 by ignoring the acetate

203 concentration-dependency terms. The comparison of RT3D simulations using Eqs. 4 and

204 Eqs. 5, as provided in Appendix B, indicated that the difference of model results was

205 negligible.

$$\frac{\partial E}{\partial t} = \mathcal{L}_E(E) + \left(\mu_{max} \frac{S}{K_S + S} - k_{decay} - k_{att} \right) E + k_{det} X + Q^s E^s \tag{5a}$$

$$\frac{\partial X}{\partial t} = \left(\mu_{max} \frac{S}{K_S + S} - k_{decay} - k_{det} \right) X + k_{att} E \tag{5b}$$

$$\frac{\partial S}{\partial t} = \mathcal{L}_S(S) - \left[\left(\frac{\mu_{max}}{Y_n} + \gamma \right) \frac{S}{K_S + S} + \frac{k_{decay}}{Y_{nd}} \right] (E + X) + Q^s S^s \tag{5c}$$

$$R \frac{\partial c}{\partial t} = \mathcal{L}_c(c) - k'(E + X)c + Q^s c^s \tag{5d}$$

206 where $R = 1 + \rho f K_d / \theta$ is the linear, instantaneous retardation factor for CT.

207   This ADRE-type model was applied to simulate a series of tests of CT biodegradation,

208   from column-scale experiments [*Witt et al.*, 1999; *Phanikumar et al.*, 2002] to field-scale

209   pilot studies [*Dybas et al.*, 1998; *Phanikumar et al.*, 2005]. This model is also used in

210   this study for comparison with simulations using the PTR method, which simulates the

211   reactions as a series of elementary steps.

3.3. Particle Tracking Method

212   The PTR method used here simulates chemical reactions through probabilistic rules of

213   particle collisions, interactions, and transformations. For a bimolecular reaction, the po-

214   tential reaction between any two particles is based on an explicit calculation of co-location

215   probability multiplied by independent thermodynamic probability that two particles react

216   upon co-location [*Benson and Meerschaert*, 2008; *Ding et al.*, 2013; *Paster et al.*, 2014].

217   Using the PTR method, the biodegradation or enzymatic reactions, as illustrated in

218   equation (1), can be simulated as a series of chemical reactions or elementary steps (2).

219   The initial bimolecular reaction that transforms the substrate to the enzyme-complex

220   (i.e., the first part of the reaction: $S + E \rightarrow ES$) is characterized by a second-order

221   kinetics: $d[S]/dt = -k_f[E][S]$. Assuming each E and S particle carries the same amount

222   of mass $m_p = \Omega[S]_0/N_S(t = 0)$, where Ω [L^d] is the domain size in d-dimensions, $[S]_0$ is the

223   average initial concentration of S [M], and $N_S(t = 0)$ is the initial number of S particles,

224   the probability comprises a co-location density function $v(s)$ and the thermodynamic

225   probability function [*Benson and Meerschaert*, 2008]:

$$P(react) = k_f \Delta t m_p v(s) \tag{6}$$

₂₂₆ where Δt is the numerical time step size and s is the separation of any pair of S and E

₂₂₇ particles.

₂₂₈ The co-location probability density function is the convolution of the individual mo-

₂₂₉ tion densities of two reactant particles (S and E) over a short time period: $v(s) =$

₂₃₀ $\int f_S(x) f_E(s + x) dx$, where $f_S(x)$ and $f_E(x)$ denote the motion densities of S and E

₂₃₁ particles away from their current positions through diffusion. Each is a Gaussian den-

₂₃₂ sity if particles diffuse under Brownian motion (see details in *Benson and Meerschaert*

₂₃₃ [2008]; *Benson et al.* [2013]). The reaction probability $P(react)$ is compared with a ran-

₂₃₄ dom number uniformly distributed between 0 and 1. If the probability of the reaction is

₂₃₅ larger than the random number, the two particles are converted to an intermediate ES

₂₃₆ complex particle. This reaction calculation requires that $k_f \Delta t m_p v(s = 0) < 1$ [*Benson*

₂₃₇ *and Meerschaert*, 2008]. Other forms of bimolecular reaction, such as $A + B \rightarrow 0$ and

₂₃₈ $A + B \rightarrow C + D$, can be simulated similarly.

₂₃₉ For the monomolecular reactions with first-order kinetics of the general form $dC/dt =$

₂₄₀ $-kC$, including the reverse dissociation reaction ($ES \rightarrow E + S$) and transform reaction

₂₄₁ ($ES \rightarrow P$), the density of particles N represents the local concentration C, thus the reac-

₂₄₂ tions can be expressed as $dN/dt = -kN$. For a small time step, Δt, the fraction change of

₂₄₃ numbers of particles is $\Delta N/N = -k\Delta t$. If the particle transitions are independent of each

₂₄₄ other, the left hand side is the probability that any particle will transform. In any time

₂₄₅ step, each particle is chosen and if $k\Delta t$ is greater than a uniform random variable $[0, 1]$,

₂₄₆ the particle is converted. This first-order kinetics simulation requires that $k\Delta t < 0.1$ for

₂₄₇ suitable accuracy.

The series of reactions (2a)-(2d), which characterize the M-M type of reaction that bacteria consume substrate and nutrients, are simulated as follows. For every time step, each E particle is selected sequentially to find nearby S particles, and the probability of co-location for each pair S and E particles is calculated. If one reaction occurs, an intermediate particle ES is placed randomly between the pair of reactant particles, which are removed. The intermediate particle ES either transforms to a product particle, or reverses to the initial S and E particles, or stays intact. These three processes are independent and are characterized with the first-order kinetics, one random number is generated to check the probability for each of the reaction processes at a time step. The impact on the reaction from the locations of released S and E particles was found to be minor [*Ding and Benson*, 2015]. Thus, we assume here that the released reactant particles are randomly distributed around the intermediate particle within a diffusion distance $\sqrt{2\boldsymbol{D}\Delta t}$.

3.4. Particle Transport Model

Our goal is to assess the differences in the transport and reaction algorithms, not to re-create the underlying hydraulics at the site. To that end, we use the exact 3-dimensional velocity fields that were generated (using MODFLOW) in the initial study [*Phanikumar et al.*, 2005]. Between each reaction step, each particle is moved based on its specific location and flow field around it using the numerical random walk particle tracking code RW3D [*Fernàndez-Garcia et al.*, 2005].

RW3D simulates solute transport by partitioning the solute mass into a large number of representative particles. The evolution of a particle's location is driven by a drift term that includes the advective movement, and a superposed Brownian motion responsible for dispersion. The displacement of a particle is modified from the Itô-Taylor integration

scheme by substituting the drift vector with modified velocity vector that includes the effects of a gradient of the dispersion tensor components [*Salamon et al.*, 2006]:

$$\boldsymbol{X}_p(t + \Delta t) = \boldsymbol{X}_p(t) + \Delta t[\boldsymbol{v}(\boldsymbol{X}_p(t)) + \nabla \cdot \boldsymbol{D}(\boldsymbol{X}_p(t))] + \sqrt{2\boldsymbol{D}(\boldsymbol{X}_p(t))\Delta t} \cdot \boldsymbol{\xi}, \qquad (7)$$

where Δt is the time step, $\boldsymbol{X}_p(t)$ is the position of a particle at time t, $\boldsymbol{v}$ is the velocity vector, $\boldsymbol{D}$ is the dispersion coefficient tensor made diagonal in the direction of transport, and $\boldsymbol{\xi}$ is a vector of independent standard normal random variables. The random walk code uses a hybrid scheme for the velocity interpolation that provides divergence-free velocity fields and a continuous dispersion tensor field that enforces mass balance at grid interfaces of adjacent cells with any degree of hydraulic conductivity contrast [*Salamon et al.*, 2006].

3.5. Schematic of Modeling Procedure

A schematic of calculation algorithm of the PTR simulations, with the developed particle tracking algorithm of reactions incorporated into the flow code, is shown in Figure 4. The growth and decay of microbe and attachment/detachment processes are also simulated as elementary steps, at the same time as chemical reactions. At any time step, the simulation follows the model procedures: i) the bacteria KC and CT experience attachment and detachment processes, which are assumed to follow a linear isotherm (see e.g. [*Benson and Bolster*, 2016]). These processes follow first-order kinetics; ii) The biomass particles are looped over to find all potential nitrate particles that may bind together into the intermediate complex in the presence of sufficient amount of electron donor, acetate, as described in Section 3.3; iii) The complex either transforms to the product, reverses back to the reactants, or stays as the complex intact. If the intermediate complex particle

²⁹⁰ transforms to a product, the bacteria particle is released; at the same time, the bacteria

²⁹¹ grow at the rate of growth yield. If the reverse reaction occurs, a substrate and a biota

²⁹² particle are regenerated. iv) Concurrently with reactions between biomass and substrate

²⁹³ (ii and iii), the degradation of CT by bacteria is simulated as a bimolecular reaction. v)

²⁹⁴ The biomass is also experiences decay. The decay term is simulated as the first-order

²⁹⁵ kinetics related to mass/concentration of bacteria. vi) The mobile particles move via

²⁹⁶ random walks after the elementary steps to the next time step.

²⁹⁷   The elementary steps and model parameters, as quantified in Eqs. 5, are listed in

²⁹⁸ Table 1. Reactions also occur to immobile particles (including the attached KC and

²⁹⁹ adsorbed CT), similar as those steps shown in Figure 4. However, the probability function,

³⁰⁰ particularly the co-location density, for the bimolecular reaction is modified to account

³⁰¹ for the immobility of attached particles, as described by *Ding and Benson* [2015].

4. Results and Discussion

4.1. Kinetic Parameters

³⁰²   The PTR model uses kinetic parameters from batch experiments directly in the simula-

³⁰³ tion. As introduced in Section 2.1, a series of batch experiments under different conditions

³⁰⁴ were conducted to estimate the reaction rates prior to the column- and field-scale studies.

³⁰⁵ The batch parameters used for the simulation are tabulated in Table 2. For instance, in

³⁰⁶ evaluating the role of trace metals on CT degradation rate, *Tatara et al.* [1993] found that

³⁰⁷ the second-order rate coefficient decreased as culture age increased from 48 to 72 hours,

³⁰⁸ which were the time for the culture to grow for the inoculation [*Dybas et al.*, 1995; *Del C.*

³⁰⁹ *Sepulveda-Torres et al.*, 1999]. *Phanikumar et al.* [2002, 2005] reported the reaction rate

³¹⁰ as 2.70 L mg^{-1}day^{-1} by taking the reaction rate for cultures aged 72 hours and grown

311 under iron-limiting conditions without the precipitate in [*Tatara et al.*, 1993]. In addi-

312 tion, the microbial decay rate, which is the only parameter not measured directly, was

313 from literature, however, the value was shown to be applicable in the simulation of CT

314 biodegradation [*Phanikumar et al.*, 2002].

4.2. Simulation of the Column Experiment in *Witt et al.* [1999]

315   The capability of the PTR method for biodegradation reactions was tested first on

316 a column-scale experiment. We incorporated the PTR simulation of reactions into the

317 RW3D code to simulate the column experiment conducted by *Witt et al.* [1999], as intro-

318 duced in Section 2.1, for verification. The simulation used the procedures introduced in

319 Section 3.5, except that the mobile particles diffuse via random walks with different diffu-

320 sion coefficients for the solutes and biomass. Possibly due to the heterogeneities, whether

321 physical, biological, or chemical, the measured initial concentrations (ICs) at different

322 sampling ports at day 0 were not uniform through the column length [*Witt et al.*, 1999].

323 To represent the non-uniform initial condition, the particles were assigned individually in

324 the 12 sections, which are separated by the 10 ports, based on the concentrations mea-

325 sured at adjacent ports. Figures 5a and 5b show the simulations of PTR model for CT

326 and nitrate, respectively, at days 2 and 26. This heterogeneous IC is reflected in the asym-

327 metric concentrations at later time. We ran 150 simulations and obtained the smoothed

328 concentration profiles by simple binning of particle numbers to account for the stochastic

329 nature of the simulations. The plots reflect the mean values plus or minus one standard

330 deviation. With the total domain initial number of particles of 3,300, 2,640, and 13 (pro-

331 portional to the initial concentrations) assigned to nitrate, biomass, and CT, the PTR

332 model in RW3D when populated with the batch rate parameters showed good matches of

measured concentrations in the column experiment. The simulation was consistent with [*Ding and Benson*, 2015], in which the same column experiment was simulated with the PTR model in a Matlab code.

In contrast, the ADRE type of model (Eq. (5)) needed to adjust the effective kinetic parameters to match column measurements [*Phanikumar et al.*, 2002; *Ding and Benson*, 2015]. In particular, because of incomplete mixing and lower apparent transport rates, the fitted CT reaction rate k' was reduced more than an order-of-magnitude, from 2.70 to 0.189 L mg^{-1}day^{-1}. Additionally, the decay rate of microbes was increased from 0.10 to 0.221 day^{-1}, and the detachment coefficient was changed from 0.018 to 0.043 day^{-1}. In a later column experiment under flowing conditions [*Phanikumar and Hyndman*, 2003], the degradation rate of CT was lowered further to 0.121 L mg^{-1}day^{-1}. The comparison of kinetic parameters values are listed in Table 2.

4.3. Simulation of Field-scale Non-reactive Tracer Test

As shown in the previous section (4.2) and in [*Ding and Benson*, 2015], the PTR method was able to simulate the relatively small degree of upscaling from batch to column scales without adjusting reaction rates. The reduced degree of mixing was achieved by fitting the particle numbers. These numbers should be exactly determined by the concentration autocorrelation function(s) [*Paster et al.*, 2014]. Because this data is available for the field site, we hypothesize that the particle method can accurately simulate the field experiment without adjusting any rate parameters from their thermodynamics, batch-scale values, as long as the velocities are well represented by the particles. This hypothesis follows from an analysis of the subgrid velocity and concentration fluctuation terms in the ADRE that need to be accounted for to numerically track imperfect mixing (D).

355   Prior to bioremediation at the Schoolcraft site, a non-reactive tracer test using bromide

356 was conducted for 20 days [*Phanikumar et al.*, 2005]. For the first five hours, groundwater

357 was pumped out of the odd numbered wells (D01, D03, ..., D15) at a total rate of

358 approximately 9.085 m^3/hr. The extracted water, with the addition of Br^- at different

359 concentrations (from 14 to 18 mg/L), was injected into the even numbered wells (D02,

360 D04, ..., D14), see the locations of wells in Figure 1. Then approximately 9.085 m^3

361 groundwater was pumped out of the even-numbered wells for one hour and injected back

362 into the odd-numbered wells after Br^- was added at the concentration of 23.5 mg/L.

363 After the pumping-injection cycle, the natural flow condition was maintained until day

364 20. The breakthrough curves of Br^- were recorded at five monitoring wells (9, 10, 11, 12,

365 and 13, as shown in Figure 1) each with five slotted intervals of 0.609 m at depths of 10.7

366 m, 13.7 m, 16.8 m, 19.84 m, and 22.9 m bgs, respectively [*Hyndman et al.*, 2000]. These

367 depths correspond to approximately 35, 45, 55, 65, and 75 feet below ground surface,

368 which was how the five intervals were named.

369   *Phanikumar et al.* [2005] used MODFLOW on the grid shown in Figure 1b to calcu-

370 late heads and discharges. On the same grid, they applied the RT3D model, a mixed

371 Lagrangian and Eulerian finite-difference (FD) implementation of the ADRE, to simulate

372 the transport of the tracer. The advection is (mostly) performed by particles in the hybrid

373 method of characteristics (HMOC), but the dispersion and reaction operations are per-

374 formed by averaging particle concentrations back to a grid for standard FD calculations.

375 Through calibration, they found that the RT3D model with a longitudinal dispersivity

376 value of 0.01 m and effective porosity of 0.3 matched the field measurements. The rel-

377 atively small dispersion coefficient implied that the variations of velocity were captured

378 with the heterogeneous and nonstationary kriged hydraulic conductivity field. Moreover,

379 the relatively rapid breakthrough of tracer (and higher mass recovery) in the deeper re-

380 gion, and slow and low concentration breakthrough in the shallow region reflected the

381 different hydraulic conductivity zones.

382 Using the exact same velocities from the MODFLOW model, we simulated the bromide

383 tracer transport using the RW3D model. The re-circulation process was simulated as

384 extracting particles within a radius of 0.1 m of pumping wells and transferring them to

385 the injection wells. The injected particles were distributed randomly within the screened

386 interval of injection wells with probability based on the flux rates at different depths. The

387 PTR method simulated the injection, re-circulation, and transport of $94,100$ particles

388 representing the total mass of 94.1 grams of Br^- in the system. We chose the number for

389 the balance of simulation variations and the computation time for a single run, because

390 the numbers of particle do not affect the average of simulated results in the conservative

391 tracer simulation. A small number of particles would lead to a high variation of the

392 simulations, but less computation time for each run. Through model tests, the number

393 of particles used ($94,100$) based on the assumption that each particle carries 1 mg mass

394 was sufficient to obtain a smooth curve of simulation.

395 The mean breakthrough curves (normalized by a concentration of 30 mg/L) from an

396 ensemble of 50 PT (RW3D) simulations match somewhat better than those of RT3D model

397 (Fig. 6). In particular, the total mass recovery is better for the PT method in 16 of the 25

398 observation locations, and the RMSE is lower in 24 of the 25 locations (Fig. 6). The means

399 of the ensemble of PT models are used in the comparison. Mass recovery is calculated

400 using the Matlab function *trapz*, which calculates the area under a set of concentration

data by breaking the region into trapezoids. The RMSE is the square root of the sum

of square differences between simulations and measurements. When these values are not

coincident in time, the simulation values are interpolated to the measurement times using

Matlab *interp1* function. It is important to stress that we seek to compare RW3D and

RT3D when reactions are included, so that we have not tried to make the new model fit

the Br^- data any better. The better fits are simply a result of zero numerical dispersion

and a better representation of incomplete mixing in the PTR model—this feature tends

to keep the Br^- more separated in layers than the FD model can simulate.

Through a limited trial-and-error effort, we found that RW3D performed well enough

with a longitudinal dispersivity value of 0.03 m, which is larger than that of RT3D model

(0.01 m). The difference is due to either numerical dispersion generated from discretization

in the FD scheme and/or recirculation well concentration calculation methods. Regarding

to the first point, finer mesh or sub-scale grid models (e.g., regridding the RT3D model)

might allow the dispersivities to match, but that effort is irrelevant to this study. The

RT3D concentrations of groundwater pumped out from wells were weighted by the hy-

draulic conductivity of model cells that the pumping wells penetrate, rather than trans-

missivity, which overestimated the contribution from the layers with small thicknesses

and underestimated the contribution from layers with large thicknesses. However, the

two models match the measurements remarkably well, so that the RW3D model can be

applied to the bioremediation experiment to assess the effect of maintaining batch-scale

reaction rates in the field-scale model.

4.4. Simulation of the field-scale bioremediation

Our goal here is to compare the Eulerian and PTR methods, so we duplicate as closely as possible the modeling efforts of *Phanikumar et al.* [2005]. We incorporated the reactions listed in Eqs. (5) into the RW3D code to simulate the field-scale CT biodegradation. The initial condition and boundary conditions were consistent with those in the RT3D model [*Phanikumar et al.*, 2005]. As described in Section 2.2, the aquifer had a plume of CT at concentrations from 1.23 to 42.9 μg/L and nitrate concentrations from 21.62 mg/L to 44.25 mg/L from 10.6 m bgs to the top of the aquitard (27.3 m bgs). The RW3D model simulates the transport of CT and nitrate without any reaction for the first 67 days. At this point, the inoculation medium (with KC and acetate) was added, the bacteria then consume nitrate and acetate to grow and biodegrade CT. Thoughout the bioremediation, the pumping-injection recirculation scheme was conducted as described in Section 2.3 and 4.3 (see details in [*Phanikumar et al.*, 2005]).

Regarding the initial conditions for the particle simulations, *Paster et al.* [2014] showed that the number of particles is directly related to the "smoothness" of the initial concentrations, as given by the autocovariance functions of the concentration fluctuations. In other words, the particles represent concentration fluctuations as well as the mean, so the number is important for accurate reactant interaction probabilities (see Appendix A). They equated the effective correlation function for the Dirac-delta particles and the covariance function of measured concentration data C to find that the particle density (in d-dimensions) should follow $\rho \approx \bar{C}_0^2/(\sigma_C^2 l^d)$, where $\bar{C}_0$ is the mean concentration, σ_C^2 is concentration variance, and l^d is the autocorrelation volume, or the integral of the correlation function in d-dimensions. Ideally, the CT concentrations from groundwater samples would be used to estimate the autocovariance function. We only have the CT

concentrations that were kriged from the original data and used in the RT3D model. We calculated the autocovariance function from these initial conditions separately in the horizontal and vertical directions (Appendix A). In the vertical direction, we estimated an average particle density of approximately 2 particles per meter. In the horizontal direction, we estimated a much lower density (because of greater correlation lengths in the horizontal space) of approximately 0.1 to 0.3 particles per square meter. To save computation time, only initial concentrations within the well field area were considered. The appropriate well field area was determined by MODFLOW capture zone analysis (traced by backward tracking of inert particles), which suggested that only the area $0 < x < 42$ m, $15 < y < 41$ m, and $2 < z < 20$ m are inside the influence of the well field for the duration of this test. So the volume of aquifer in which we simulate transport and reaction is 42 m $\times$ 26 m in area $\times$ 18 m thick and must contain an initial distribution of $4,000$ to $12,000$ CT particles based on the CT spatial statistics (Appendix A).

One main objective using the PTR method is to evaluate if the observed overall reduced reaction rates in the field scale can be attributed to the incomplete mixing. Therefore, the PTR model within RW3D used all prior laboratory (batch) parameters. This is different from the RT3D model, which overpredicted degradation significantly using the laboratory CT reaction rate k'.

Because the concentration of injected acetate (electron donor) was more than 20 times higher (800 versus 30 mg/L) than that of nitrate (electron acceptor), the concentration profile of acetate was reported to resemble that of non-reactive tracer Br^-, even though a small amount of acetate is consumed during the reactive transport [*Witt et al.*, 1999; *Phanikumar et al.*, 2005]. Hence, for the sake of brevity, we only show the comparison

468 of simulated and observed concentrations of CT and nitrate at monitoring wells. The

469 simulation results include those from the RT3D model from [*Phanikumar et al.*, 2005] and

470 the PTR method within RW3D. Concentrations of CT and nitrate were measured at wells

471 9, 10, 11, 12 and 13 at five observation depths, 10.7 m, 13.7 m, 16.8 m, 19.84 m, and 22.9 m

472 bgs. The breakthrough curves of CT and nitrate were normalized with concentrations of

473 0.032 and 42 mg/L, respectively [*Phanikumar et al.*, 2005]. The measured and simulated

474 breakthrough curves of CT and nitrate are plotted in Figures 7 and 8, respectively.

475 Given the estimated range of initial number of CT particles from auto-covariance analy-

476 sis, we ran simulation tests by varying the mass each particle carries (m_p) and found that

477 the initial particles number of $4,612$ — on the lower-end of the range of $4,000$ to $12,000$

478 — provided a good match of concentration profiles. The low end was derived based on

479 ignoring the hole effect when integrating CT autocovariance, which may be a numerical

480 artifact. In other words, the particle number is more closely associated with the estima-

481 tion of positive correlation. The total number of initial sorbed CT particles was calculated

482 as $27,460$ based on distribution coefficients at different layers [*Dybas et al.*, 2002]. The

483 number of nitrate particles within the influence area of the well field was calculated as

484 $2,867,400$. The distribution of the initial particles was calculated from individual concen-

485 trations at each MODFLOW model cell and the mass each particle carries (see details in

486 Appendix C1). During the inoculation, 471 KC particles were added. The number of KC

487 particles grew rapidly, especially in the attached phase, so that 100 days after inoculation

488 approximately 1,760 detached and 76,000 attached KC particles were present in the model

489 domain. In addition, the consumption of nitrate by the native flora was assumed to occur

490 where the nutrient (acetate) and nitrate were both available. We also assumed, as did

491   *Phanikumar et al.* [2002], that the population of native flora is proportional to that of KC.

492   The calculated number of microbe particles representing the native bacteria is described

493   in Appendix C2. This is different from the simulation of the column experiment, where

494   we assumed that the impact of native microbes was negligible because the column was

495   flushed 4 weeks to achieve a denitrifying condition [*Witt et al.*, 1999]. However, measure-

496   ments of nitrate in the field suggested that the consumption rate of nitrate was beyond

497   the capability of the limited amount of KC injected (see also [*Phanikumar et al.*, 2005]).

498   To account for the stochastic nature of the PTR method, we ran 50 simulations to

499   obtain a smoothed curve for simulated concentrations, and plotted the mean $\pm$ one stan-

500   dard deviation (Figs. 7 and 8). Based on the analysis of moving averages at randomly

501   selected sampling times for all wells from the 50 realizations, we found that the relevant

502   statistics of the simulations at most wells converged at around 30 to 40 realizations, as

503   shown in Appendix E. Similar to the Br^- breakthrough curves, good matches between

504   measured and PTR simulated nitrate and CT are found in all the monitoring well loca-

505   tions. Simulated concentrations from both models in the upper low K zone were generally

506   lower than those of observations, especially at the depth of 13.7 m (45 ft), similar to the

507   breakthrough curves of bromide, as shown in Figure 6. This implies that the preferential

508   flow was not fully captured in the MODFLOW flow field, particularly in the low K zone.

509   This under-prediction might also be due to the kriging method interpolating hydraulic

510   conductivities, which smoothed the variability of K.

511   As also shown in Figures 7 and 8, the standard deviation of the simulated results in

512   some zones was relatively large. This is because the fast moving or easy reacting particles

513   may or may not captured in the small counting bins (capture zone) of individual wells in

different model runs. The randomness of the numbers of particles reflects the imperfect

mixing condition. If an infinite number of particles, which represents a complete mixing

condition, were used for the simulation, the variance would be close to zero and we would

expect results similar to the Eulerian model. In other words, the finite number of particles

accounts for the degree of mixing in the site (Appendix D), which explains why the

apparent reaction rate was more than one order of magnitude lower in the field than in

the lab.

The over-prediction of CT reaction rates by the RT3D model using laboratory-optimized

rates was explained through the availability of electron acceptor and limitation of micro-

bial growth at the field scale [*Phanikumar et al.*, 2005]. These factors contribute to the

overall process of reactants mixing at a range of scales. To match the field measure-

ments, *Phanikumar et al.* [2005] increased the kinetic attachment value and lowered the

CT degradation rate. In contrast, the PTR model did not adjust the kinetic parameters;

instead, the number of particles, which represents the mass of solutes and biomass, as

well as the variability of concentrations within a fixed volume, were estimated to account

for the incomplete mixing [*Benson et al.*, 2013].

Moreover, attachment/detachment process combined with the difference of degradation

capability between the mobile and immobile microbes were thought to lead to the increase

in CT observed in the high conductivity layers for some wells after the post-inoculation

decline (e.g., well 10-75 at 22.9 m (75 ft) depth) [*Phanikumar et al.*, 2005]. Because only

limited information is available for the difference of reaction rate constants between mobile

and immobile bacteria, the reaction rates are assumed to be constant for both phases,

as used in the RT3D model [*Phanikumar et al.*, 2005]. During the inoculation period (2

hours), the attachment coefficient for bacteria was increased by one order of magnitude in *Phanikumar et al.* [2005]. In the PTR method, the attachment coefficient is kept constant and equal to the laboratory-measured values. We have assumed that 90% of the microbes are attached on the aquifer material during injection. This is consistent with previous studies on bacteria transport and field observations [*Ding*, 2010; *Dybas et al.*, 2002].

As shown in Figures 7 and 8, the biodegradation of CT and consumption of nitrate during the field-scale bioremediation are well-simulated using the PTR method with batch-scale parameters. The RMSE of the simulations from the two numerical models were calculated for both CT and nitrate. By this measure, The PTR method better predicted the CT concentration breakthrough curves in 23 of 25 wells (Fig. 7). On the other hand, the PTR method predicted a slower decline, or consumption rate, of nitrate. This is most likely because we assigned the numbers of particles based on the autocovariance of initial CT concentrations. To maintain stoichiometry, a very large number of nitrate particles were needed, which may or may not represent the spatial heterogeneity of the nitrate initial condition. The large number implies that nitrate consumption is not limited by mixing due to its high concentration and smoothness. This smoothness is reflected in the gradual overall breakthrough of nitrate in many wells in the PTR simulations. The PTR model results also show more high-frequency variability in the BTC, which represent the impact of re-circulation (pump/inject) process on the concentrations. On the contrary, the RT3D model provides smooth lines that could be the result of numerical dispersion (especially vertical mixing). The better nitrate RMSE fit is evenly split (12 to 13) between the two models.

5. Discussion and Conclusions

This study presents a series of novel developments, including the first implementation of complex reaction kinetics at the field-scale using a purely Lagrangian particle transport and reaction (PTR) code. The reasons for implementing such a code are primarily: 1) to avoid the spurious mixing that grid-based Eulerian algorithms can impart; and 2) represent subgrid velocity and concentration perturbations. The difficulty that grid-based codes have in accurately simulating the degree of mixing between chemical species is accurately handled by the particle methods [*Benson et al.*, 2017; *Herrera et al.*, 2017].

The column experiment of CT biodegradation that was performed in support of the Schoolcraft field-scale experiment is simulated using the PTR method within RW3D. Kinetics parameters from batch experiments were directly used in this method. The results are consistent with those from the PTR simulation using a Matlab code, as presented by *Ding and Benson* [2015]. Observed concentration profiles at 10 sampling ports at both day 2 and 26 were closely matched with most measurements within one standard deviation of the ensamble mean. This contrasts with Eulerian simulations of the columns, which required reductions of CT degradation rate parameter from 2.70 to 0.189 L mg^{-1}day^{-1} [*Ding and Benson*, 2015]. The column experiment simulation suggests that the PTR method within RW3D can simulate CT biodegradation, which involves processes of first-order, second-order, and Monod-type reactions, as well as attachment/detachment, growth and decay of biomass. The upscaling of mixing that accompanied moving to the column scale was handled by the particle method through the calibration of particle numbers. These numbers are dictated by the chemical autocovariance functions that were not measured at the beginning of the column test.

581   On the other hand, the statistics of the CT initial condition were measured at the

582   Schoolcraft field site. The input files to RT3D from the study of *Phanikumar et al.* [2005]

583   gave us an estimate of the covariance functions, and we calculated the initial particle

584   numbers prior to PTR simulations of bioremediation.

585   Before running those simulations, we simulated the transport of bromide tracer test at

586   the Schoolcraft site using particle tracking (RW3D) and the same velocities as an RT3D

587   model. The RW3D simulations matched Br^- measurements with a longitudinal disper-

588   sivity value of 0.03 m, which is about 3 times larger than that used in the RT3D model.

589   Due to the lack of numerical dispersion that arises from transferring back and forth from

590   Lagrangian and Eulerian schemes, the RW3D model better matches the breakthrough

591   curves in most observation wells.

592   Finally, we applied the PTR model to simulate the site bioremediation. The simulation

593   involved the processes of solute and bacteria transport, attachment/detachment, growth

594   and decay of biomass, as well as the reactions among CT, bacteria KC, electron donor (ac-

595   etate), and electron acceptor (nitrate). The comparison between simulated and measured

596   breakthrough curves at 25 monitoring well locations, as well as the comparison between

597   RT3D and RW3D simulations, indicate that the PTR method can accurately simulate the

598   field experiment without adjusting any parameters from the batch scale, particularly the

599   CT biodegradation rate, which needed to be reduced by a factor of 22 in the RT3D model

600   [*Phanikumar et al.*, 2005]. However, the success of the PTR method requires accurate

601   velocity fields and an accurate assessment of the spatial autocovariance of the reactant

602   initial condition, because these factors are the primary controls of potential mixing and

603   dictate the number of particles used in the domain.

We previously mentioned the large number of sites that have shown the scale effect of reaction rates. One source is chemical heterogeneity, especially subgrid or unrepresented fluctuations. Another source has gotten more recent attention: the ADRE contains only one term that must simultaneously account for both spreading and mixing of solutes (e.g., *Kapoor et al.* [1998]; *Battiato et al.* [2009]; *Le Borgne et al.* [2010]; *Dentz et al.* [2011]; *Le Borgne et al.* [2013]; *de Anna et al.* [2014]; *Porta et al.* [2016]). Only at the very smallest scales are these two quantities of similar magnitudes. As solutes encounter more heterogeneous Darcy velocities, the spreading grows faster than the local mixing. For the ADRE to accurately describe spreading, it must overpredict mixing and vice-versa: accurate representation of mixing will under-disperse solutes and place reactants in the wrong places. A corollary is that perfectly homogeneous sites (i.e., $\text{VAR}(\ln(K) \to 0)$) would not suffer from this particular effect. A notable example of a reactive transport experiment in relatively homogeneous material is the petroleum hydrocarbon injection/biodegradation experiment in the Borden aquifer [*Schirmer et al.*, 2000]. With $\text{VAR}(\ln(K)) = 0.244$, *Schirmer et al.* [2000] were able to use laboratory-estimated M-M parameters in a finely-discretized field-scale model to accurately simulate aerobic degradation of injected contaminants (under natural gradient conditions). For comparison, the Schoolcraft aquifer's overall $\text{VAR}(\ln(K)) = 0.634$, about 2.6 times greater than Borden's. Because 2nd-order (including M-M) or higher reactions introduce a nonlinear amplification into any transport errors [*Benson et al.*, 2017], we conclude that the scale effect due to velocity fluctuations will manifest at all but the most homogeneous sites. Going from $\text{VAR}(\ln(K)) = 0.244$ to 0.634 appears to have made a significant difference, although there were other differences in the two experiments that may have contributed, including aerobic versus anaerobic con-

ditions, small and relatively homogeneous injected contaminant volumes at the Borden

site, and the natural-flow versus forced-recirculation conditions.

In the present study, we used the original PTR method from [*Benson and Meerschaert*, 2008], which requires that all reactant particles carry the same amount of mass. Because of the large difference in concentrations of CT and nitrate, a very large number of nitrate particles ($\approx$ 3 million) were assigned in the simulation and thus it requires a large computational effort relative to the prior RT3D model (approximately 22 versus 4 hours on a 3.4 GHz i7-3770 processor with 24 Gb RAM). However, new PTR methods address the problem of large particle numbers and discrepancies, by either allowing particles to have variable mass [*Bolster et al.*, 2016; *Benson et al.*, 2017], allowing particles to carry multiple species [*Benson and Bolster*, 2016], or larger "footprints" by using kernels with optimal particle influence instead of the current Dirac-delta functions [*Fernàndez-Garcia and Sanchez-Vila*, 2011; *Rahbaralam et al.*, 2015; *Schmidt et al.*, 2017]. Much shorter computation times should be expected with these methods and a more rigorous benchmarking of the current study could be performed.

In summary, the PTR method with RW3D is capable of simulating field-scale bioremediation with equal or better accuracy than traditional methods. Furthermore, the reaction parameters transfer from the smallest scale, separating the scale-dependence of reaction rates from the underlying source of reduced reaction: poor mixing at larger scales.

Appendix A: Estimation of intial CT particle numbers (density)

Estimation of the CT autocovariance function is performed on the input files for RT3D, which has 39 non-zero layers. In the horizontal direction, the autocovariance is calculated individually in each layer using standard methods and assuming isotropy with respect to

₆₄₉ lag separation. Data pairs were grouped in lag intervals (0 0.5), (0.5 1.5), (1.5 2.5), ...

₆₅₀ (23.5 24.5). A plot of each layer's estimated autocovariance function versus radial lags is

₆₅₁ shown in figure A1. Also plotted is the layer-thickness weighted average autocovariance,

₆₅₂ which has a summed correlation function (which includes the "hole effect" of negatively

₆₅₃ correlated values) of $l = 3.2$ m. Ingoring the negative values gives a visual estimate of

₆₅₄ the correlation length on the order of 5 m. Extending to 2-d, it is safe to say that the

₆₅₅ 2-d correlation volume is on the order of 10 to 30 m^2. The total CT mean and variance

₆₅₆ within the non-zero layers in the RT3D input file are 0.0127 and 5.3×10^{-5}, respectively,

₆₅₇ so that the average initial particle density (see *Paster et al.* [2014] for a derivation) in the

₆₅₈ horizontal is $\rho = \bar{C}^2/(\sigma^2 l^d) \approx 3/l^d \approx 0.3$ to 0.1 particle per square meter. In the vertical,

₆₅₉ more noise was resolved, and the average autocovariance function has a 1-d correlation

₆₆₀ length of about 1.5 m (Fig. A2), so that the average particle density in the vertical

₆₆₁ direction is about 2 particles per meter.

Appendix B: Modification on the ADRE-based model and differences in the simulation

₆₆₂   In the ADRE-based model in [*Phanikumar et al.*, 2005], as listed in Eqs. 4, a correction

₆₆₃ factor $[1 - A/(K_A + A)]$ was added to the bacteria decay term to account for the increase

₆₆₄ of decay rate at low nutrient concentration [*Beeftink et al.*, 1990; *Phanikumar et al.*, 2005].

₆₆₅ However, *Beeftink et al.* [1990] proposed this correction term because they considered the

₆₆₆ growth and decay of biomass together (or net growth) in their study. Moreover, during

₆₆₇ the bioremediation in the Schoolcraft field, the concentration of acetate was nearly three

₆₆₈ orders of magnitude higher than the half saturation constant (800 mg/L versus. 1 mg/L)

and acetate has been continuously added to the system, the correction term was always close to zero in the well field. This results in nearly no decay in the equation.

To assess the effect of the modification from Eqs. 4 to Eqs. 5, we ran the RT3D model with both equations in parallel. As shown in Figures B1 and B2, the differences using these two equations were minor, especially at locations with high concentrations (lower part), RT3D simulations using the two equations were nearly overlapped. This is because the concentration of injected acetate (electron donor) was more than 20 times higher (800 versus 30 mg/L) than that of nitrate (electron acceptor). Moreover, it is common in field bioremediation systems that more electron donor (e.g., acetate) than needed is added to promote the initiation of the reactions [*Alexander*, 1999; *Dybas et al.*, 1998; *Finneran et al.*, 2002; *Anderson et al.*, 2003; *Williams et al.*, 2011]. As reported by *Witt et al.* [1999] and *Phanikumar et al.* [2005], the concentration profile of acetate resembles that of Br^-, even though a small amount of acetate is consumed during the reactive transport. Similarly, the correction factor applied to the detachment term has negligible effect on the simulations.

Appendix C: Correlation of particle numbers with initial concentrations and injections

C1. Initial concentrations

Initially, CT and nitrate were present in the groundwater system. In the PTR simulation, initial numbers of CT and nitrate particles were calculated based on the concentrations from the RT3D model and groundwater volumes.

C1.1. CT in groundwater

The observed CT values were divided into six layers ($28 - 15.5$ m, $15.5 - 11.5$ m, $11.5 - 8$ m, $8 - 5$ m, $5 - 2$ m, and $2 - 0$ m bgs, respectively) and kriged as separate zones [*Phanikumar et al.*, 2005].

The RT3D model has the kriged CT initial concentrations (c_i), which were used directly to calculate the number of particles at each MODFLOW/RT3D model cell. The total number of particles is based on the total mass of CT in groundwater, M_{CT}:

$$M_{CT} = \sum_{i=1}^{r \times n \times l} c_i \cdot V_i \cdot \theta \tag{C1}$$

where V_i = finite-difference cell volume; θ = porosity; r = number of rows in the model; n = number of columns in the model; and l = number of layers in the model. The total number of CT particles is pre-determined by the the autocovariance (Appendix A), i.e., N_{CT} is within the range of 4000 to $12,000$. Model simulations suggested that simulations with $N_{CT} = 4,612$ provided a reasonable match of measurements, so the the mass of each particle of each species is given by

$$m_p = \frac{M_{CT}}{N_{CT}} \tag{C2}$$

The concentration of CT was from 0 to 0.00429 mg/L. The total mass was calculated as 371.04 g. The mass within the influence area of the well field was about 73.3 g and the mass each particle carries is 0.016 g.

C1.2. Sorbed CT

The initial sorbed CT is assumed to be in equilibrium of aqueous CT. The distribution coefficients were reported vary with the depth, from 0.145 to 0.353 L/kg [*Dybas et al.*, 2002; *Phanikumar et al.*, 2005]. The numbers of sorbed CT particles are calculated from

the aqueous CT concentration and distribution coefficients at different depth.

$$M_{S_{CT}} = \frac{c \cdot K_d \cdot \rho_b}{\theta} = \sum_{i=1}^{r \times n \times l} \frac{c_i \cdot K_{dl} \cdot \rho_b}{\theta} \qquad (C3)$$

The number of sorbed CT particles would be Eq. C4.

$$N_{S_{CT}} = \frac{M_{S_{CT}}}{m_p} \qquad (C4)$$

C1.3. Nitrate

Initial nitrate concentrations were fairly constant across the region, the layer averaged concentrations were used for the current simulation. The number of particles used for initial nitrate in the system is calculated similarly as that of CT.

$$N_{Nitrate} = \frac{M_{Nitrate}}{m_p} = \frac{S \cdot V \cdot \theta}{m_p} \qquad (C5)$$

The concentration of nitrate at each layer are constant, thus, the calculation of mass is conducted on layers, instead of model cells. The concentrations were found ranging from 21.62 mg/L to 44.25 mg/L from 10.6 m bgs to 27.4 m bgs. Linear interpolation is used to assign nitrate concentration to different layers. The mass of initial nitrate was calculated as $116,514$ g within a smaller influence zone of the well field with length of 41.43 m, width of 14.4 m, and the effective porosity of 0.3. Model tests indicated that a smaller zone for nitrate did not affect the simulation results due the uniform distribution of nitrate, but it saved the computational time.

C2. Injected mass

During inoculation, at day 67, the concentrations of KC and acetate injected to the biocurtain were 10^6 CFU/mL and 800 ppm, respectively [*Phanikumar et al.*, 2005]. Certain numbers of particles were simulated to be injected based on the fluxes of injection and the addition of constituents.

725   The injection contained the concentrations of KC at 10^6 CFU/mL, while 1 CFU/ mL

726   is approximately equal to 1.67×10^{-7} ppm for strain KC [*Phanikumar et al.*, 2002], thus,

727   the concentration of KC in the injection was 0.167 mg/L.

728   The total number of KC particles added to the injection wells is given by:

$$N_{KC} = \frac{M_{KC}}{m_p} = \frac{E \cdot Q_{inj} \cdot t}{m_p} = \frac{\sum_{i=1}^{15} \sum_{j=1}^{2} E_{i,j} \cdot Q_{inj_{i,j}} \cdot t_j}{m_p}, \qquad (C6)$$

729   where M_{KC} = mass of KC injected through the inoculation, $Q_{inj,j}$ = volume of groundwa-

730   ter injected to well i at period j, and t_j is the duration of injection at period j. The time

731   steps 45 and 47 had the duration of 0.05555 and 0.04514 day, respectively, with injection

732   volumes were approximately 12 m^3 and 9.75 m^3, respectively. The number of acetate

733   particles is proportional to the nitrate particles based on the ratio of concentrations in

734   the injection of re-circulation processes, which were 800 mg/L for acetate and 30 mg/L

735   for nitrate. After inoculation, acetate concentration injected were one order-of-magnitude

736   lower, 80 mg/L.

C3. Consumption of Nitrate by indigenous microflora

737   The consumption of nitrate by the native flora was assumed to occur where acetate was

738   available. The consumption is represented with parameter γ. Even though endogenous

739   respiration is the process by which microbes consume cell reserves in the absence of an

740   electron donor (acetate) and continue to use an electron acceptor (nitrate), we use the

741   same assumption that *Phanikumar et al.* [2002] made, which states that the population

742   of native flora is proportional to that of KC.

743   *Phanikumar and Hyndman* [2003] estimated the γ term as 18.89 day^{-1}. Based on

744   the model of nitrate consumption in *Phanikumar et al.* [2005], the proportion of native

₇₄₅ flora over KC is related to the ratio of γ over μ_{max}/Y_n. Given the laboratory-obtained

₇₄₆ specific growth rate (nitrate utilization rate), $\mu_{max} = 3.11 day^{-1}$, and the yield for nitrate,

₇₄₇ $Y_n = 0.25$ mg cells/mg substrate. The population of native microflora would be 4.554

₇₄₈ times greater than KC.

Appendix D: Perturbation analysis

₇₄₉ We adopt the methodology of *deAnna et al.* [2011], *Tartakovsky et al.* [2012], and *Paster*

₇₅₀ *et al.* [2014] to examine the components of the ADRE that contribute to reduced effective

₇₅₁ reaction rates and to assess whether the Lagrangian method is an appropriate tool to sim-

₇₅₂ ulate these components. Assume that the ADRE with bimolecular reaction has random

₇₅₃ components v, C_A, and C_B with means denoted by overbars and zero-mean fluctuations

₇₅₄ denoted by primes. For simplicity we assume that the local dispersion is relatively con-

₇₅₅ stant:

$$\frac{\partial(\bar{C}_i + C'_i)}{\partial t} = -\nabla \cdot [(\bar{v} + v')(\bar{C}_i + C'_i) + D\nabla(\bar{C}_i + C'_i)] - k(\bar{C}_A + C'_A)(\bar{C}_B + C'_B). \quad \text{(D1)}$$

₇₅₆ Taking the ensemble mean,

$$\frac{\partial \overline{C}_i}{\partial t} = -\nabla \cdot [\bar{v}\overline{C}_i - D\nabla\overline{C}_i + \overline{v'C'_i}] - k(\overline{C}_A\overline{C}_B + \overline{C'_A C'_B}). \quad \text{(D2)}$$

₇₅₇ So to first order, the new terms relative to the ADRE are a macrodispersion term and a

₇₅₈ modification of the macroscopic reaction rate by the concentration cross-covariance as in

₇₅₉ the case of purely diffusive transport [*Tartakovsky et al.*, 2012; *Paster et al.*, 2014]. It is

₇₆₀ worth discussing each of the terms on the right hand side of (D2) with respect to "subgrid"

₇₆₁ quantities. The mean advection and local dispersion of the of the mean concentration

₇₆₂ (the first and second terms) as well as the reaction of the mean concentrations (the

₇₆₃ fourth term) are the only terms solved at a grid scale by typical Eulerian transport codes.

Particle methods also represent these mean velocities and mean concentrations. However, the subgrid velocity perturbations are also solved by particles [*Herrera et al.*, 2017], i.e., velocities are interpolated between grid velocities to particles depending on their position within a cell [*LaBolle et al.*, 1996]. Therefore, shear, compression and dilation (all of which contribute to mixing and reaction [*de Barros et al.*, 2012; *Engdahl et al.*, 2014]) can be tracked by particles within cells. Furthermore, properly defined, the particles can also represent concentration perturbations at any scale as demonstrated by *Paster et al.* [2014] and *Schmidt et al.* [2017]. It is also worth noting that no study has examined the solution of (D2) by particles in the most general cases, but several have looked at simpler systems where the velocity perturbations are known functions of space. In particular, *Porta et al.* [2012a] examined Poiseuille flow in which v' is parabolic across an aperture, and *Porta et al.* [2012b, 2013] did numerical volume averaging in an idealized unit cell. The former study showed that the particle method was an accurate simulator of the volume-averaged reacting system. The latter study showed that naively upscaled ADRE equations will follow the reaction-rate scaling that we seek to eliminate by representing subgrid fluctuations. To isolate the term that modifies the reaction rate in (D2), first subtract the mean from the total equation:

$$\frac{\partial C_i'}{\partial t} = -\nabla \cdot [\overline{v} C_i' + v' \overline{C}_i + v' C_i' + \overline{v' C_i'} - D\nabla C_i'] + k\overline{C_A' C_B'} - k(\overline{C}_A C_B' + \overline{C}_B C_A' + C_A' C_B'). \quad \text{(D3)}$$

Now take (D3) for $i = A$ multiplied by C_B' and add to (D3) for $i = B$ multiplied by C_A'. Discarding third-order in perturbation terms and using fluid incompressibility yields

$$\frac{\partial C_A' C_B'}{\partial t} = -\overline{v} \cdot \nabla C_A' C_B' + D\nabla^2 C_A' C_B' - C_B' v' \cdot \nabla \overline{C}_A - C_A' v' \cdot \nabla \overline{C}_B - 2D\nabla C_B' \cdot \nabla C_A'$$

$$- k(\overline{C}_A C_B'^2 + \overline{C}_B C_A' C_B' + \overline{C}_B C_A'^2 + \overline{C}_A C_A' C_B'). \text{(D4)}$$

783   Define $g = \overline{C'_A C'_B}$, $f_A = \overline{C'^2_A}$ and $f_B = \overline{C'^2_B}$ and taking the ensemble average of (D3)

784   gives

$$\frac{\partial g}{\partial t} = -\overline{v} \cdot \nabla g + D\nabla^2 g - \overline{C'_B v'} \cdot \nabla \overline{C}_A - \overline{C'_A v'} \cdot \nabla \overline{C}_B - 2D\overline{\nabla C'_B \cdot \nabla C'_A}$$

$$-k(\overline{C}_A f_B + \overline{C}_B g + \overline{C}_B f_A + \overline{C}_A g). \tag{D5}$$

785   Similarly for f_i $(i = A, B); j = (B, A)$

$$\frac{\partial f_i}{\partial t} = -\overline{v} \cdot \nabla f_i + D\nabla^2 f_i - 2\overline{C'_i v'} \cdot \nabla \overline{C}_i - 2D\overline{\nabla C'_i \cdot \nabla C'_i}$$

$$-2k(\overline{C}_i g + \overline{C}_j f_i). \tag{D6}$$

786   It was this system of equations, with $\overline{v} = v' = 0$, that was solved by *Paster et al.* [2014]

787   both analytically and with the particle method. They showed that the particle method was

788   more accurate in that case because it does not throw out any higher-order terms (required

789   for analytic closure). The interesting aspect of (D5) and (D6) is that the concentration

790   auto- and cross-covariances follow an advection-diffusion equation with additional "macro-

791   mixing" terms. Classic long-term closures for the terms $\overline{C'_i v'}$ for conservative tracers are

792   often assumed to take the form $D_{macro}\nabla C_i$ [*Taylor*, 1953; *Gelhar et al.*, 1979]. Inclusion

793   of these types of terms would lead to additional terms of the form $D_{macro}\nabla C_i \cdot \nabla C_j$,

794   which have been shown to represent the local mixing of constituents i and j [*Le Borgne*

795   *et al.*, 2010]. It is also worth noting that an attempt to analytically quantify the relative

796   contributions of the various terms in (D5) and (D6), which dictate the evolution of g and

797   deviations of the overall reaction rate (from (D2)), will depend in complex and spatially

798   variable ways according to local Peclet and Damkohler numbers as well as the initial

799   conditions of g and f_i.

To summarize, (D5) and (D6) show that concentration perturbations' auto- and cross-covariance are advected, dispersed, macro-mixed, micro-mixed, and source/sinked in a coupled manner. The evolution of the cross-covariance, which is responsible for the decreased overall reaction rate in (D2) is non-stationary and may be difficult to close accurately in an analytic sense. But prior (and separate) work has shown that the particle method can simulate all of the terms in these equations.

Appendix E: Plots of moving averages of the simulations

Because of the stochastic nature of the PTR simulation, a number of realizations were conducted to plot the average and standard deviation. In this study, we ran 50 simulations. To verify if the 50 realizations were sufficient to represent the stable conditions, we plotted the moving averages of nitrate concentration from the 50 realizations at three different times: before (day 30), during (day 72), and after (day 122) the injection and re-circulation process. In consideration of different average values at different wells, we plotted the ratio of difference between moving average and final average over final average: $(C_m - C_{ave})/C_{ave}$; where C_m is the moving average at realization m, C_{ave} is the average for all 50 realizations. As the graphs shown, the average of the simulations at most wells converged at around $30 - 40$ realizations. Therefore, the selection of 50 realizations was reasonable regarding to the average condition and the results were deemed stable and convergent.

As also shown in the figure C1, the variations of $(C_m - C_{ave})/C_{ave}$ for day 30 and 72 were small, generally $< 10\%$, while the variation at the late stage were larger (figure C1c). This is because the average concentration at day 122 was as low as 0.08 mg/L, which is represented by only a few particles. In different model realizations, the particles may or

may not captured in the small counting bins of individual wells. In fact, the variation of average concentration was small.

References

Alexander, M. (1999), *Biodegradation and Bioremediation*, – pp., Elsevier Science & Technology.

Anderson, R., H. Vrionis, I. Ortiz-Bernad, C. Resch, P. Long, R. Dayvault, K. Karp, S. Marutzky, D. Metzler, A. Peacock, et al. (2003), Stimulating the in situ activity of Geobacter species to remove uranium from the groundwater of a uranium-contaminated aquifer, *Applied and Environmental Microbiology*, *69*(10), 5884–5891.

Battiato, I., D. M. Tartakovsky, A. M. Tartakovsky, and T. Scheibe (2009), On breakdown of macroscopic models of mixing-controlled heterogeneous reactions in porous media, *Adv. Water Resour.*, *32*, 1664–1673, doi:10.1016/j.advwatres.2009.08.008.

Beeftink, H., R. van der Heijden, and J. Heijnen (1990), Maintenance requirements: energy supply from simultaneous endogenous respiration and substrate consumption, *FEMS Microbiology Letters*, *73*(3), 203–209, doi:10.1111/j.1574-6968.1990.tb03942.x.

Benson, D. A., and D. Bolster (2016), Arbitrarily complex chemical reactions on particles, *Water Resources Research*, *52*(11), 9190–9200, doi:10.1002/2016WR019368.

Benson, D. A., and M. M. Meerschaert (2008), Simulation of chemical reaction via particle tracking: Diffusion-limited versus thermodynamic rate-limited regimes, *Water Resour. Res.*, *44*, W12,201.

Benson, D. A., D. Bolster, and A. Paster (2013), Communication: A full solution of the annihilation reaction $A + B \rightarrow \emptyset$ based on time-subordination, *The Journal of Chemical Physics*, *138*(13), 131101.

Benson, D. A., T. Aquino, D. Bolster, N. Engdahl, C. V. Henri, and D. Fernàndez-Garcia (2017), A comparison of Eulerian and Lagrangian transport and non-

linear reaction algorithms, *Advances in Water Resources*, *99*, 15 – 37, doi: http://doi.org/10.1016/j.advwatres.2016.11.003.

Biteman, S. E., D. W. Hyndman, M. S. Phanikumar, and G. S. Weissmann (2004), Integration of sedimentalogic and hydrologic properties for improved transport simulations, in *Spec. Publ. SEPM Soc. Sediment. Geol.*, vol. 80, edited by J. Bridge and D. W. Hyndman, pp. 3–13, SEPM.

Bolster, D., P. de Anna, D. A. Benson, and A. M. Tartakovsky (2012), Incomplete mixing and reactions with fractional dispersion, *Advances in Water Resources*, *37*(0), 86 – 93.

Bolster, D., A. Paster, and D. A. Benson (2016), A particle number conserving Lagrangian method for mixing-driven reactive transport, *Water Resources Research*, *52*(2), 1518–1527, doi:10.1002/2015WR018310.

Chapelle, F., and D. Lovley (1990), Rates of microbial metabolism in deep coastal plain aquifers, *Applied and Environmental Microbiology*, *56*(6), 1865–1874.

Criddle, C. S., J. T. DeWitt, D. Grbić-Galić, and P. L. McCarty (1990), Transformation of Carbon Tetrachloride by Pseudomonas sp. strain KC under denitrification conditions., *Applied and Environmental Microbiology*, *56*(11), 3240–3246.

de Anna, P., M. Dentz, A. Tartakovsky, and T. Le Borgne (2014), Filamentary structure of mixing fronts controls reaction kinetics in porous media flows, *Geophysical Research Letters*, p. in press.

de Barros, F. P. J., M. Dentz, J. Koch, and W. Nowak (2012), Flow topology and scalar mixing in spatially heterogeneous flow fields, *Geophysical Research Letters*, *39*(8), n/a–n/a, doi:10.1029/2012GL051302, l08404.

deAnna, P., T. LeBorgne, M. Dentz, D. Bolster, and P. Davy (2011), Anomalous kinetics in diffusion limited reactions linked to non-Gaussian concentration probability distribution function, *Journal of Chemical Physics*, *135*, 174,104.

Del C. Sepulveda-Torres, L., N. Rajendran, M. J. Dybas, and C. S. Criddle (1999), Generation and initial characterization of pseudomonas stutzeri kc mutants with impaired ability to degrade carbon tetrachloride, *Archives of Microbiology*, *171*(6), 424–429, doi: 10.1007/s002030050729.

Dentz, M., T. L. Borgne, A. Englert, and B. Bijeljic (2011), Mixing, spreading and reaction in heterogeneous media: a brief review, *Journal of Contaminant Hydrology*, *120-121*, 1–17.

Ding, D. (2010), Transport of bacteria in aquifer sediment: experiments and modeling, *Hydrogeology Journal*, *18*(3), 669–679.

Ding, D., and D. A. Benson (2015), Simulating biodegradation under mixing-limited conditions using Michaelis–Menten (Monod) kinetic expressions in a particle tracking model, *Advances in Water Resources*, *76*, 109–119, doi:10.1016/j.advwatres.2014.12.007.

Ding, D., D. A. Benson, A. Paster, and D. Bolster (2013), Modeling bimolecular reactions and transport in porous media via particle tracking, *Advances in Water Resources*, *53*(0), 56–65.

Dybas, M. J., G. M. Tatara, and C. S. Criddle (1995), Localization and characterization of the Carbon Tetrachloride transformation activity of Pseudomonas sp. strain KC., *Applied and Environmental Microbiology*, *61*(2), 758–62.

Dybas, M. J., M. Barcelona, S. Bezborodnikov, S. Davies, L. Forney, H. Heuer, O. Kawka, T. Mayotte, L. Sepúlveda-Torres, K. Smalla, M. Sneathen, J. Tiedje, T. Voice, D. C.

Wiggert, M. E. Witt, and C. S. Criddle (1998), Pilot-scale evaluation of bioaugmenta-

tion for in-situ remediation of a Carbon Tetrachloride-contaminated aquifer, *Environ.*

Sci. Technol., *32*(22), 3598–3611, doi:10.1021/es980200z.

Dybas, M. J., D. W. Hyndman, R. Heine, J. Tiedje, K. Linning, D. Wiggert, T. Voice,

X. Zhao, L. Dybas, and C. S. Criddle (2002), Development, operation, and long-term

performance of a full-scale biocurtain utilizing bioaugmentation, *Environ. Sci. Technol.*,

36(16), 3635–3644, doi:10.1021/es0114557.

Engdahl, N. B., D. A. Benson, and D. Bolster (2014), Predicting the enhancement of

mixing-driven reactions in nonuniform flows using measures of flow topology, *Phys.*

Rev. E, *90*(5), 051,001–, doi:10.1103/PhysRevE.90.051001.

Fernàndez-Garcia, D., and X. Sanchez-Vila (2011), Optimal reconstruction of concentra-

tions, gradients and reaction rates from particle distributions., *Journal of contaminant*

hydrology, *120-121*, 99–114.

Fernàndez-Garcia, D., T. H. Illangasekare, and H. Rajaram (2005), Differences in the

scale-dependence of dispersivity estimated from temporal and spatial moments in chem-

ically and physically heterogeneous porous media, *Advances in Water Resources*, *28*(7),

745–759, doi:10.1016/j.advwatres.2004.12.011.

Finneran, K. T., R. T. Anderson, K. P. Nevin, and D. R. Lovley (2002), Potential for

bioremediation of uranium-contaminated aquifers with microbial U(VI) reduction, *Soil*

and Sediment Contamination: An International Journal, *11*(3), 339–357.

Gelhar, L. W., A. L. Gutjahr, and R. L. Naff (1979), Stochastic analysis of macrodis-

persion in a stratified aquifer, *Water Resources Research*, *15*(6), 1387–1397, doi:

10.1029/WR015i006p01387.

Gillespie, D. T. (1976), A general method for numerically simulating the stochastic time evolution of coupled chemical reactions, *Journal of Computational Physics*, *22*(4), 403 – 434.

Herrera, P. A., J. M. Cortínez, and A. J. Valocchi (2017), Lagrangian scheme to model subgrid-scale mixing and spreading in heterogeneous porous media, *Water Resources Research*, *53*(4), 3302–3318, doi:10.1002/2016WR019994.

Hesse, F., F. Radu, M. Thullner, and S. Attinger (2009), Upscaling of the advection-diffusion-reaction equation with Monod reaction, *Advances in Water Resources*, *32*(8), 1336–1351.

Hyndman, D. W., M. Dybas, L. Forney, R. Heine, T. Mayottee, M. Phanikumar, G. Tatara, J. Tiedje, T. Voice, R. Wallace, D. Wiggert, X. Zhao, and C. Criddle (2000), Hydraulic characterization and design of a full-scale biocurtain, *Ground Water*, *38*(3), 462–474, doi:10.1111/j.1745-6584.2000.tb00233.x.

Kapoor, V., C. T. Jafvert, and D. A. Lyn (1998), Experimental study of a bi-molecular reaction in Poiseuille flow, *Water Resour. Res.*, *34*(8), 1997–2004, doi: 10.1029/98WR01649.

Kehew, A. E., W. T. Straw, W. K. Steinman, P. G. Barrese, G. Passarella, and W.-S. Peng (1996), Ground-water quality and flow in a shallow glaciofluvial aquifer impacted by agricultural contamination, *Ground Water*, *34*(3), 491–500, doi:10.1111/j.1745-6584.1996.tb02030.x.

King, E., K. Tuncay, P. Ortoleva, and C. Meile (2010), Modeling biogeochemical dynamics in porous media: Practical considerations of pore scale variability, reaction networks, and microbial population dynamics in a sandy aquifer, *Journal of Contaminant Hydrol-*

ogy, *112*(1–4), 130–140.

LaBolle, E. M., G. E. Fogg, and A. F. B. Tompson (1996), Random-walk simulation of transport in heterogeneous porous media: Local mass-conservation problem and implementation methods, *Water Resour. Res.*, *32*(3), 583–593.

Le Borgne, T., M. Dentz, D. Bolster, J. Carrera, J. de Dreuzy, and P. Davy (2010), Non–Fickian mixing: Temporal evolution of the scalar dissipation rate in heterogeneous porous media, *Adv. Water Res.*, *33*(12), 1468–1475.

Le Borgne, T., M. Dentz, and E. Villermaux (2013), Stretching, coalescence, and mixing in porous media, *Physical Review Letters*, *110*(20), 204,501.

Lohse, K. A., P. D. Brooks, J. C. McIntosh, T. Meixner, and T. E. Huxman (2009), Interactions between biogeochemistry and hydrologic systems, *Annual Review of Environment and Resources*, *34*, 65–96, doi:10.1146/annurev.environ.33.031207.111141.

Mayotte, T. J., M. J. Dybas, and C. S. Criddle (1996), Bench-scale evaluation of bioaugmentation to remediate Carbon Tetrachloride-contaminated aquifer materials, *Ground Water*, *34*(2), 358–367, doi:10.1111/j.1745-6584.1996.tb01896.x.

Meile, C., and K. Tuncay (2006), Scale dependence of reaction rates in porous media, *Advances in Water Resources*, *29*(1), 62–71.

Michaelis, L., and M. L. Menten (1913), Die kinetik der invertinwirkung, *Biochem. z*, *49*(333-369), 352.

Monod, J. (1949), The growth of bacterial cultures, *Annu. Rev. Microbiol.*, *3*(1), 371–394.

Paster, A., D. Bolster, and D. A. Benson (2014), Connecting the dots: Semi-analytical and random walk numerical solutions of the diffusion-reaction equation with stochastic initial conditions, *Journal of Computational Physics*, *263*, 91–112.

Pedretti, D., D. Fernàndez-Garcia, D. Bolster, and X. Sanchez-Vila (2013), On the formation of breakthrough curves tailing during convergent flow tracer tests in three-dimensional heterogeneous aquifers, *Water Resour. Res.*, *49*(7), 4157–4173, doi: 10.1002/wrcr.20330.

Phanikumar, M. S., and D. W. Hyndman (2003), Interactions between sorption and biodegradation: Exploring bioavailability and pulsed nutrient injection efficiency, *Water Resour. Res.*, *39*(5), doi:10.1029/2002WR001761.

Phanikumar, M. S., D. W. Hyndman, D. C. Wiggert, M. J. Dybas, M. E. Witt, and C. S. Criddle (2002), Simulation of microbial transport and Carbon Tetrachloride biodegradation in intermittently-fed aquifer columns, *Water Resour. Res.*, *38*(4), 4–1–4–13.

Phanikumar, M. S., D. W. Hyndman, X. Zhao, and M. J. Dybas (2005), A three-dimensional model of microbial transport and biodegradation at the Schoolcraft, Michigan, site, *Water Resour. Res.*, *41*(5), W05,011–.

Porta, G., G. Ceriotti, and J.-F. Thovert (2016), Comparative assessment of continuum-scale models of bimolecular reactive transport in porous media under pre-asymptotic conditions, *Journal of Contaminant Hydrology*, *185–186*, 1 – 13, doi: 10.1016/j.jconhyd.2015.12.003.

Porta, G. M., J.-F. Thovert, M. Riva, A. Guadagnini, and P. M. Adler (2012a), Microscale simulation and numerical upscaling of a reactive flow in a plane channel, *Phys. Rev. E*, *86*(3), 036,102–.

Porta, G. M., M. Riva, and A. Guadagnini (2012b), Upscaling solute transport in porous media in the presence of an irreversible bimolecular reaction, *Advances in Water Resources*, *35*, 151–162, doi:10.1016/j.advwatres.2011.09.004.

Porta, G. M., S. Chaynikov, J.-F. Thovert, M. Riva, A. Guadagnini, and P. M. Adler (2013), Numerical investigation of pore and continuum scale formulations of bimolecular reactive transport in porous media, *Advances in Water Resources*, *62, Part B*, 243–253, doi:10.1016/j.advwatres.2013.09.007.

Rahbaralam, M., D. Fernàndez-Garcia, and X. Sanchez-Vila (2015), Do we really need a large number of particles to simulate bimolecular reactive transport with random walk methods? a kernel density estimation approach, *Journal of Computational Physics*, *303*, 95–104, doi:10.1016/j.jcp.2015.09.030.

Rubin, S., I. Dror, and B. Berkowitz (2012), Experimental and modeling analysis of coupled non-Fickian transport and sorption in natural soils, *Journal of Contaminant Hydrology*, *132*(0), 28–36.

Salamon, P., D. Fernàndez-Garcia, and J. J. Gómez-Hernández (2006), A review and numerical assessment of the random walk particle tracking method, *Journal of Contaminant Hydrology*, *87*(3–4), 277–305, doi:10.1016/j.jconhyd.2006.05.005.

Scheibe, T. D., R. Mahadevan, Y. Fang, S. Garg, P. E. Long, and D. R. Lovley (2009), Coupling a genome-scale metabolic model with a reactive transport model to describe in situ uranium bioremediation, *Microbial Biotechnology*, *2*(2), 274–286.

Schirmer, M., J. W. Molson, E. O. Frind, and J. F. Barker (2000), Biodegradation modelling of a dissolved gasoline plume applying independent laboratory and field parameters, *Journal of Contaminant Hydrology*, *46*, 339–374.

Schmidt, M. J., S. Pankavich, and D. A. Benson (2017), A kernel-based Lagrangian method for imperfectly-mixed chemical reactions, *Journal of Computational Physics*, *336*, 288 – 307, doi:http://doi.org/10.1016/j.jcp.2017.02.012.

Scholl, M. A. (2000), Effects of heterogeneity in aquifer permeability and biomass on biodegradation rate calculations—results from numerical simulations, *Ground Water*, *38*(5), 702–712.

Steefel, C. I., D. J. DePaolo, and P. C. Lichtner (2005), Reactive transport modeling: An essential tool and a new research approach for the earth sciences, *Earth and Planetary Science Letters*, *240*(3–4), 539–558.

Tan, Y., J. T. Gannon, P. Baveye, and M. Alexander (1994), Transport of bacteria in an aquifer sand: Experiments and model simulations, *Water Resour. Res.*, *30*(12), 3243–3252, doi:10.1029/94WR02032.

Tartakovsky, A. M., P. de Anna, T. Le Borgne, A. Balter, and D. Bolster (2012), Effect of spatial concentration fluctuations on effective kinetics in diffusion-reaction systems, *Water Resour. Res.*, *48*(2), W02,526–.

Tatara, G. M., M. J. Dybas, and C. S. Criddle (1993), Effects of medium and trace metals on kinetics of Carbon Tetrachloride transformation by Pseudomonas sp. strain KC., *Applied and Environmental Microbiology*, *59*(7), 2126–2131.

Taylor, G. (1953), Dispersion of soluble matter in solvent flowing slowly through a tube, *Proceedings of the Royal Society of London A: Mathematical, Physical and Engineering Sciences*, *219*(1137), 186–203, doi:10.1098/rspa.1953.0139.

Tufenkji, N. (2007), Modeling microbial transport in porous media: Traditional approaches and recent developments, *Advances in Water Resources*, *30*(6-7), 1455–1469, doi:10.1016/j.advwatres.2006.05.014.

Waite, T. R. (1957), Theoretical treatment of the kinetics of diffusion-limited reactions, *Phys. Rev.*, *107*, 463–470.

Williams, K. H., P. E. Long, J. A. Davis, M. J. Wilkins, A. L. N'Guessan, C. I. Steefel, L. Yang, D. Newcomer, F. A. Spane, L. J. Kerkhof, L. McGuinness, R. Dayvault, and D. R. Lovley (2011), Acetate availability and its influence on sustainable bioremediation of Uranium-contaminated groundwater, *Geomicrobiology Journal*, *28*(5-6), 519–539.

Witt, M. E., M. J. Dybas, R. M. Worden, and C. S. Criddle (1999), Motility-enhanced bioremediation of Carbon Tetrachloride-contaminated aquifer sediments, *Environ. Sci. Technol.*, *33*(17), 2958–2964.

Yabusaki, S. B., Y. Fang, K. H. Williams, C. J. Murray, A. L. Ward, R. D. Dayvault, S. R. Waichler, D. R. Newcomer, F. A. Spane, and P. E. Long (2011), Variably saturated flow and multicomponent biogeochemical reactive transport modeling of a Uranium bioremediation field experiment, *Journal of Contaminant Hydrology*, *126*(3–4), 271–290.
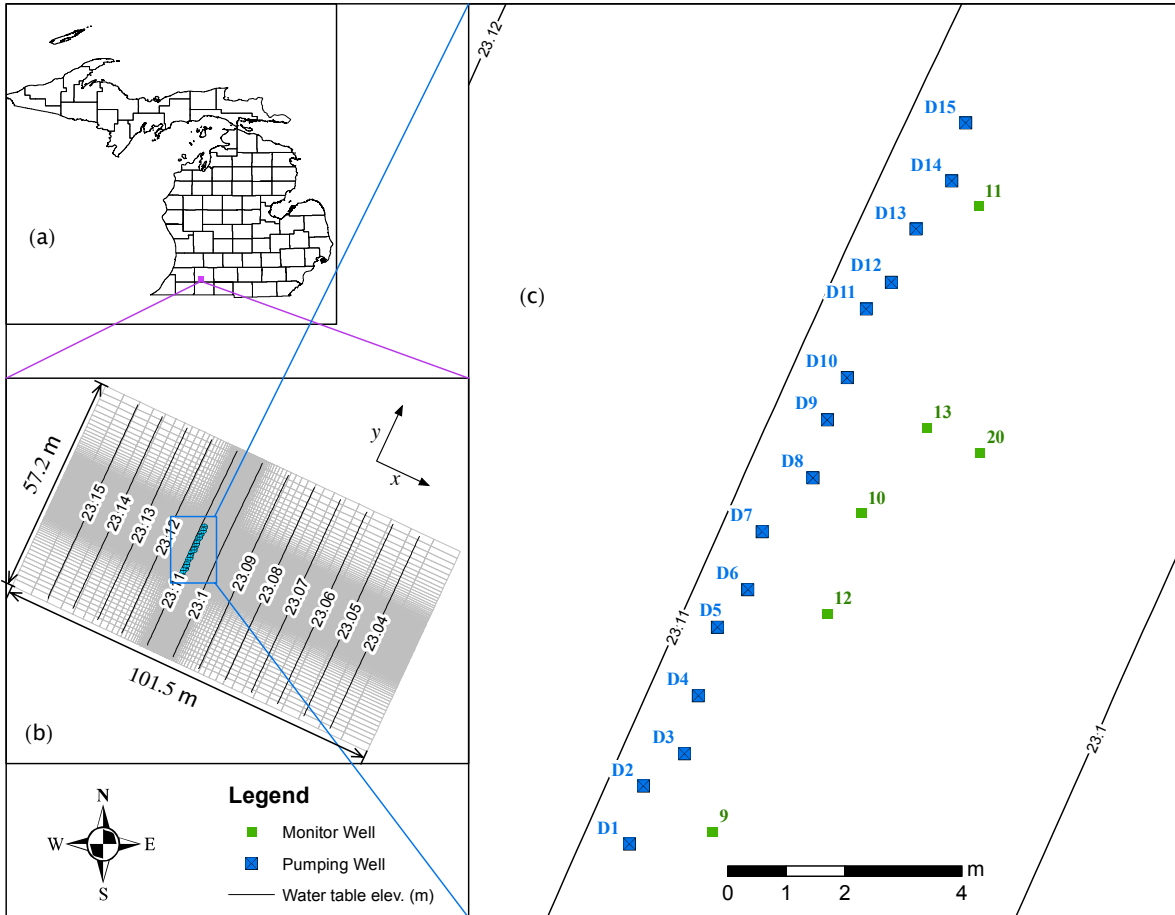
Figure 1. a) Location of the project site in Michigan, USA; b) Prior MODFLOW and RT3D model domain, finite-difference cells, and coordinate system (after [*Phanikumar et al.*, 2005]); c) Delivery wells of the bioaugmentation system (*D*1 to *D*15), and multi-level monitoring wells 9, 10, 11, 12, 13, and 20.
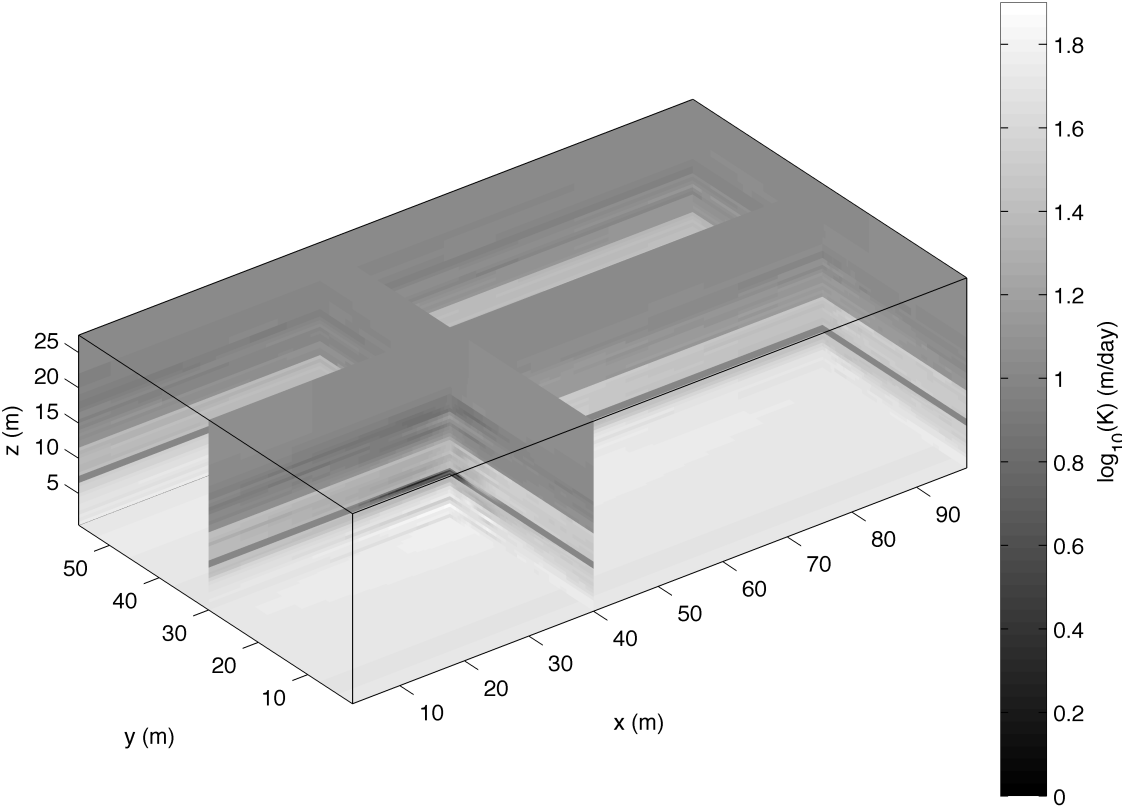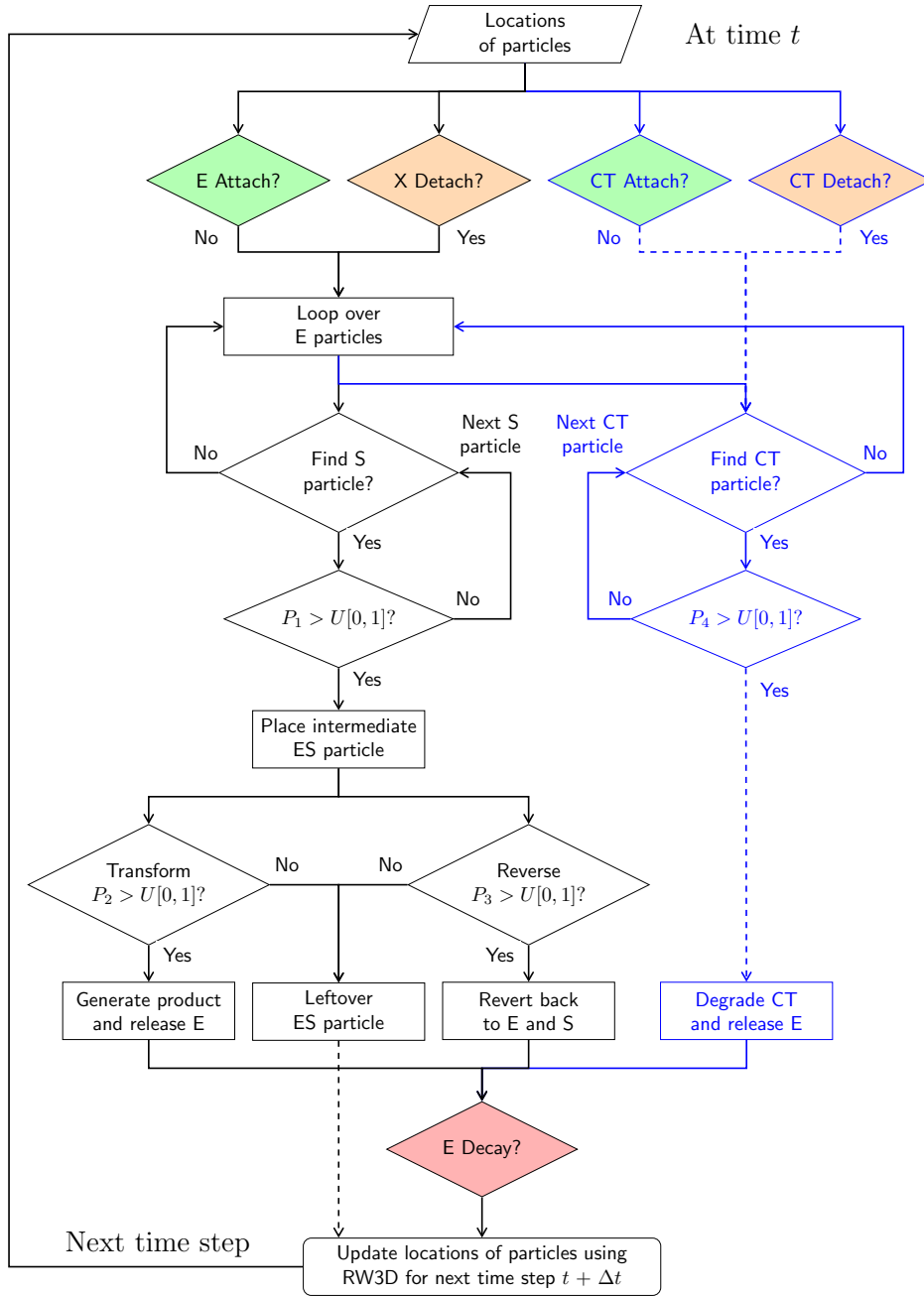
Figure 2.   Kriged hydraulic conductivity field in the model domain.
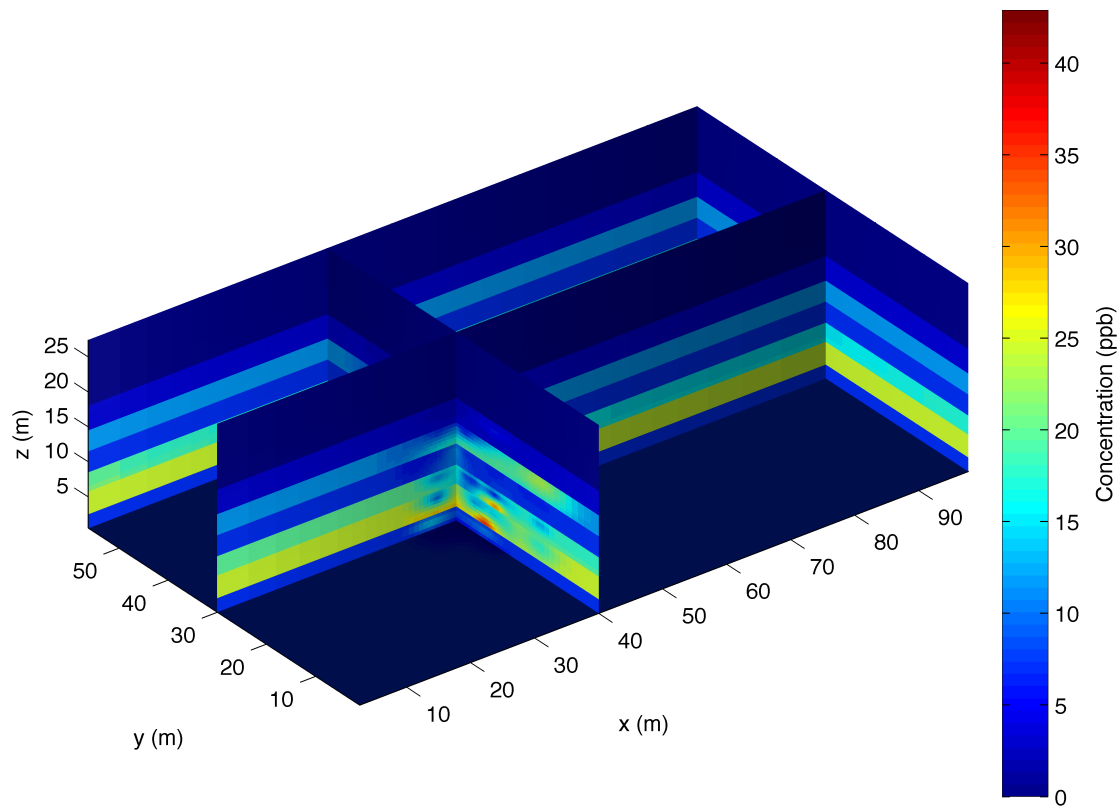
Figure 3.   Interpolated (kriged) initial CT concentrations within the model domain.

The autocovariance of these RT3D inputs guide the density of CT particles placed in the

PTR model simulations.

Figure 4. Flow chart of PTR simulation of substrate S and biomass E reactions in the aqueous phase. For each time step, the particles go through the series of reaction process (2a)-(2d), including the biodegradation of CT, as described in Section 3.3, P_1, P_2, P_3, and P_4 in the chart represent the probability for the specific step. The attachment and detachment process and growth and decay of biomass are simulated as elementary steps. The locations of particles are updated via RW3D model based on the locations of particles and the flow field around the particles, as described in Section 3.4.

Table 1. Elementary steps of the reactions

| Step	Equation	Parameter
Adsorption of CT	$c \rightarrow c_S$	k_{ads} [1]
Desorption of CT	$c_S \rightarrow c$	k_{des}
Attachment of mobile bacteria KC [2]	$E \rightarrow X$	k_{att}
Detachment of immobile bacteria KC [2]	$X \rightarrow E$	k_{det}
Nitrate binds to mobile bacteria	$S + E \rightarrow ES$	k_s [3]
Nitrate binds to immobile bacteria	$S + X \rightarrow XS$	k_s [3]
CT biodegradation by mobile bacteria	$c + E \rightarrow P$ [4]	k'
CT biodegradation by immobile bacteria	$c + X \rightarrow P$ [4]	k'
Bacteria biodegrade adsorbed CT	$c_S + E \rightarrow P$ [4]	k'
Intermediate ES reverts to nitrate and mobile KC	$ES \rightarrow S + E$	k_r
Intermediate XS reverts to nitrate and immobile KC	$XS \rightarrow S + X$	k_r
Transformation of ES and growth of mobile KC	$ES \rightarrow (1 + Y)E + p$ [5]	k_c
Transformation of XS and growth of immobile KC	$XS \rightarrow (1 + Y)X + p$ [5]	k_c
Decay of mobile bacteria KC	$E \rightarrow 0$	k_{dec}
Decay of immobile bacteria KC	$X \rightarrow 0$	k_{dec}

[1] The rate is calculated based on the fraction of exchange sites and distribution coefficient. Linear isotherm is assumed.

[2] Indigenous microflora are assumed to have the same steps as KC.

[3] The reaction rates involving indigenous microflora are calculated based on the ratio of γ and μ_{max} in Eq. (5).

[4] P represents the product of CT biodegradation.

[5] Y is the growth yield of biomass, and p is the products of nitrate transformation.
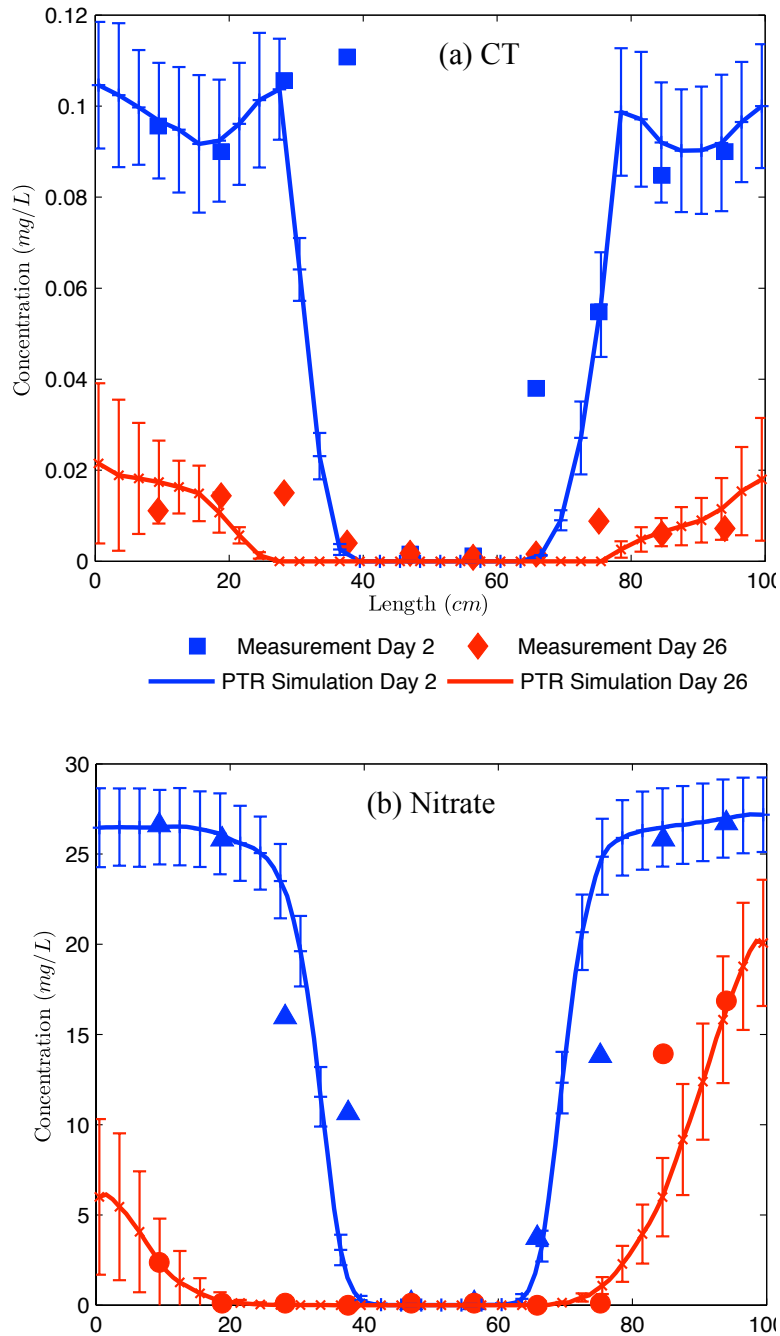
Figure 5. Measured (symbols) and simulated (lines with error bars) concentrations at day 2 and day 26 using RW3D and experiments from *Witt et al.* [1999]. (a) Carbon tetrachloride (CT) and (b) Nitrate. The lines with error bars are means plus and minus one standard deviation of 150 simulations using the PTR method implemented in RW3D.

**Table 2.**   Laboratory Measured and ADRE Model Fitted Parameters for CT Biodegradation.

Parameter	Symbol	Units	Batch Value	Column-Fitted	Field-Fitted
Biodegradation rate	k'	L mg^{-1} d^{-1}	2.70	0.189	0.121
Maximum specific growth rate	μ_{max}	d^{-1}	3.11	3.11	3.11
Nitrate utilization by microflora	γ	d^{-1}	0.0	18.89	18.89
Microbial decay rate	k_{decay}	d^{-1}	0.1 [a]	0.13	0.00016 [b]
Attachment coefficient	k_{att}	d^{-1}	–	0.9	0.9 / 9 [c]
Detachment coefficient	k_{det}	d^{-1}	–	0.018	0.04
Growth yield for nitrate	Y_n	–	0.25	0.25	0.25
Growth yield for biomass	Y_{nd}	–	0.46	0.46	0.46
Half saturation coefficient of nitrate	K_m	mg/L	12.0	12.0	12.0
Binding rate constant	k_f	L mg^{-1} d^{-1}	0.36 [d]	–	–

[a] The value is from literature, as noted in *Phanikumar, 2002.*

[b] The decay rate was converted from Eq. 4 to first-order decay rate in Eq. 5 by multiplying the acetate correction factor for comparison.

[c] 10 times higher attachment coefficient was used during the inoculation period ([*Phanikumar et al.*, 2005]).

[d] This rate, calculated from [*Tatara et al.*, 1993], is used only in elementary reaction steps but not in the Monod equation.
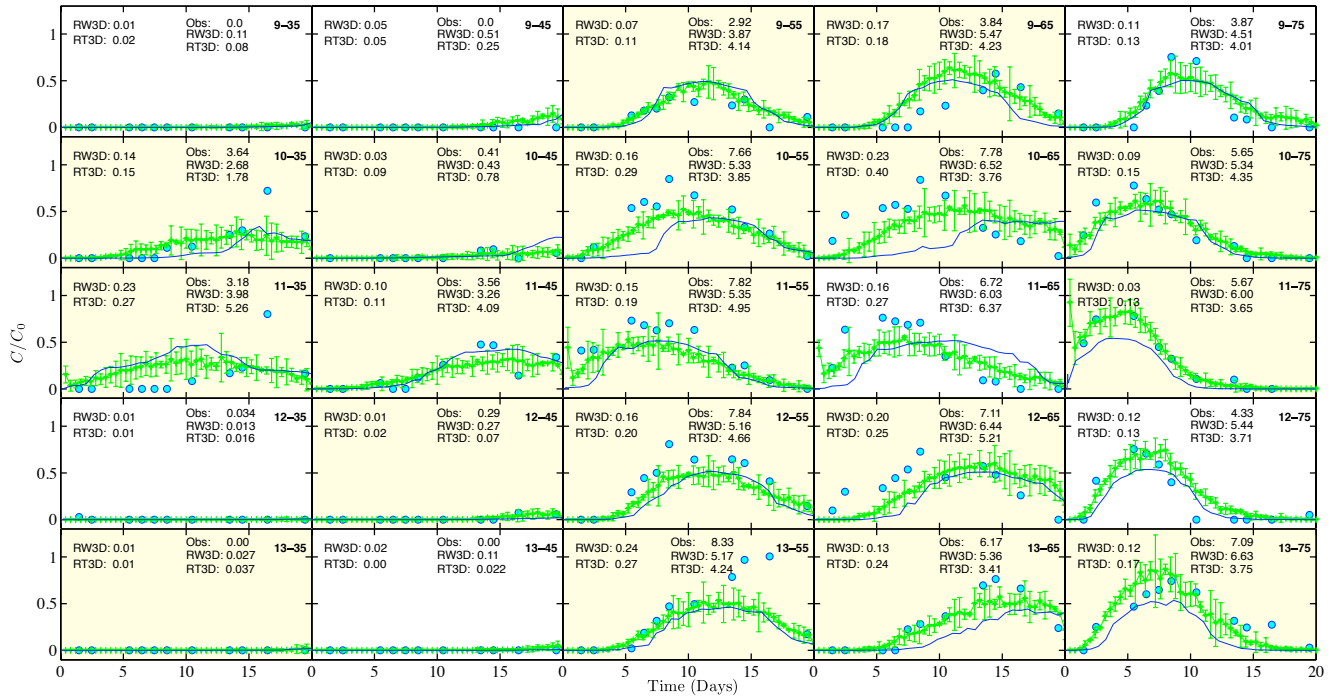
Figure 6. Measured and simulated breakthrough curves of Bromide. The symbols are measured concentrations; the blue lines are simulations using RT3D, and the green lines with error bars are simulated results from RW3D model. The error bars are plus/minus one standard deviation from 50 realizations. Bold, dashed numbers denote well and sampling depth (ft bgs). The numbers on the left are the RMSE from RT3D model and RW3D model compared to the measurements, respectively. The right side labels are the mass recovery from measurements, RT3D, and RW3D, respectively. The sub-figures in which the PT simulations match better than, or equal to, those of ADRE-type model are highlighted in yellow.
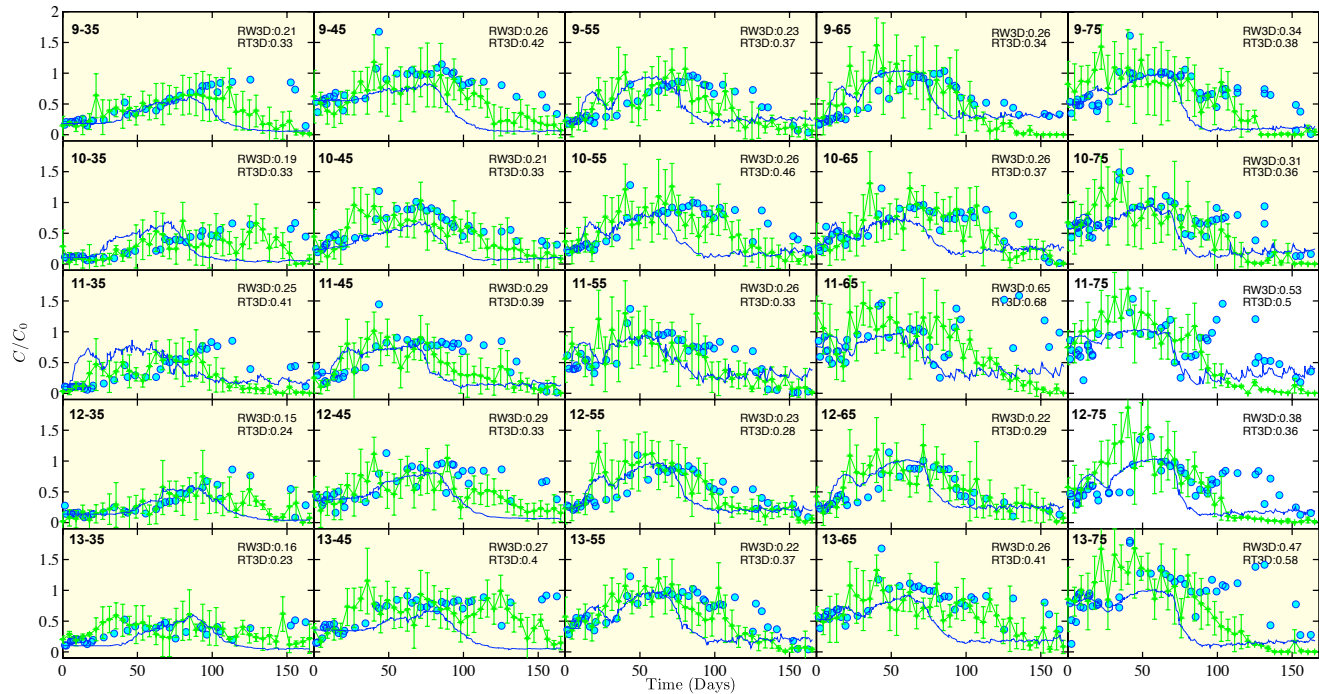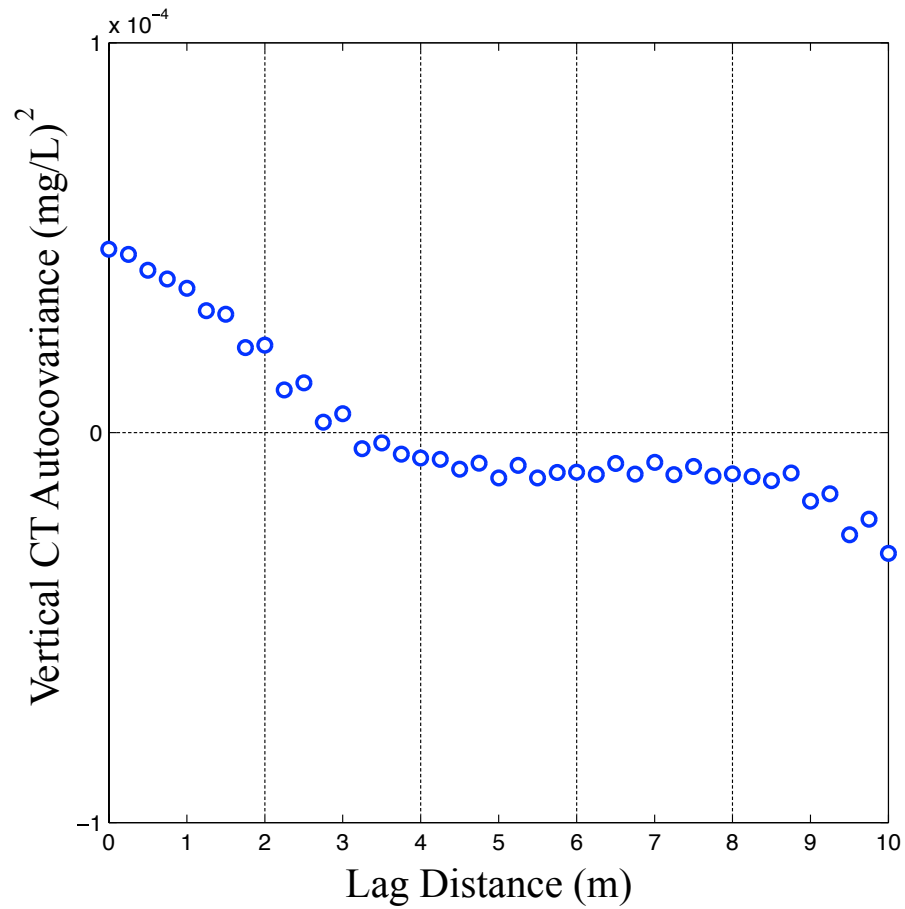
Figure 7. Measured and simulated breakthrough curves of CT. The circles are the measured concentrations, the blue lines are simulations using RT3D, and the green lines with error bars are the means plus/minus one standard deviation from 50 simulations of the PTR method in RW3D. Bold, dashed numbers denote well and sampling depth (ft bgs). Numbers reflect RMSE differences between modeled and measured normalized concentrations, and wells with better PTR simulations are given a yellow background.
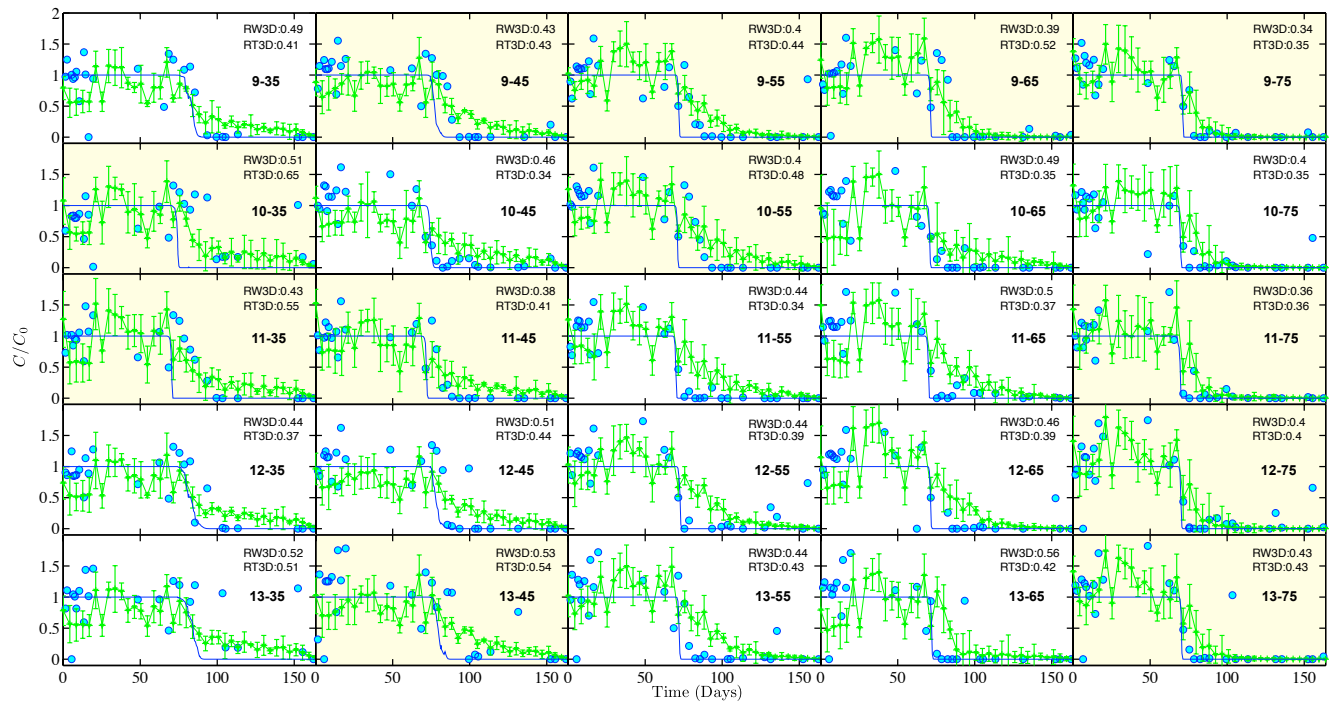
Figure 8. Measured and simulated breakthrough curves of nitrate. The circles are the measured concentrations in five wells at five depths, the blue lines are simulations using RT3D, and the green lines with error bars are the means plus/minus one standard deviation from 50 simulations of the PTR method in RW3D. Bold, dashed numbers denote well and sampling depth (ft bgs). Numbers reflect RMSE differences between modeled and measured normalized concentrations, and wells with better PTR simulations are given a yellow background.
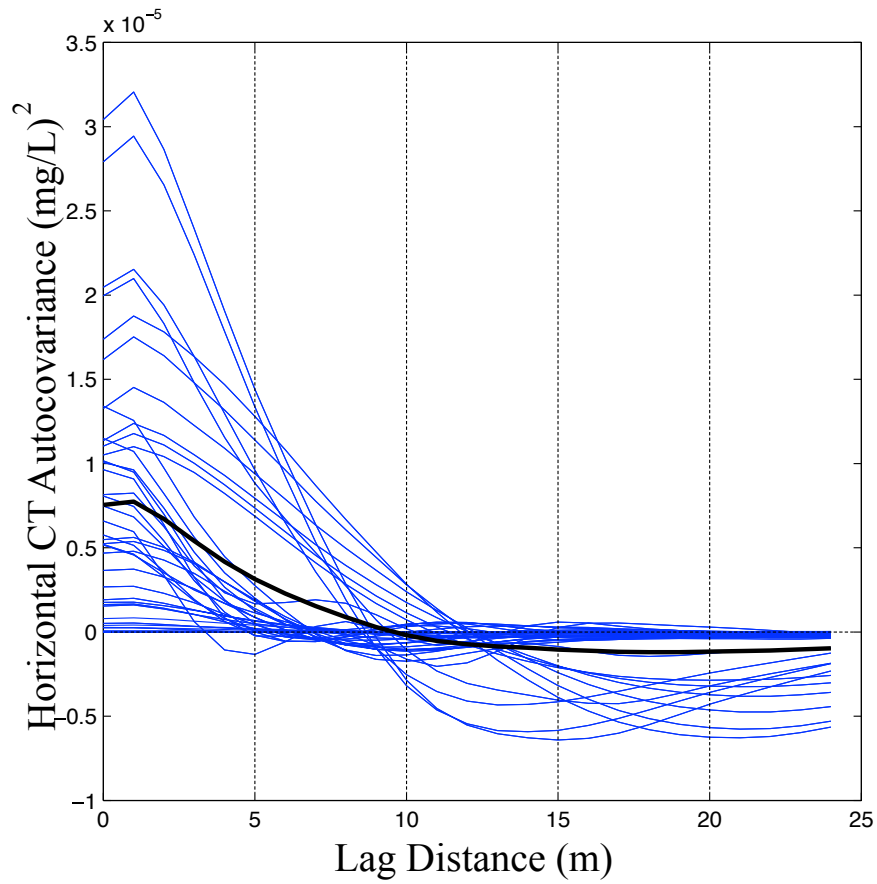
Figure A1. Estimated horizontal autocovariance functions in each of 39 non-zero layers from the initial CT concentrations from the RT3D file [*Phanikumar et al.*, 2005]. The thickness weighted average of the layers is shown with a thick black line.

Figure A2. Estimated vertical autocovariance functions for CT in the entire model domain using the initial CT concentrations from the RT3D file [*Phanikumar et al.*, 2005].
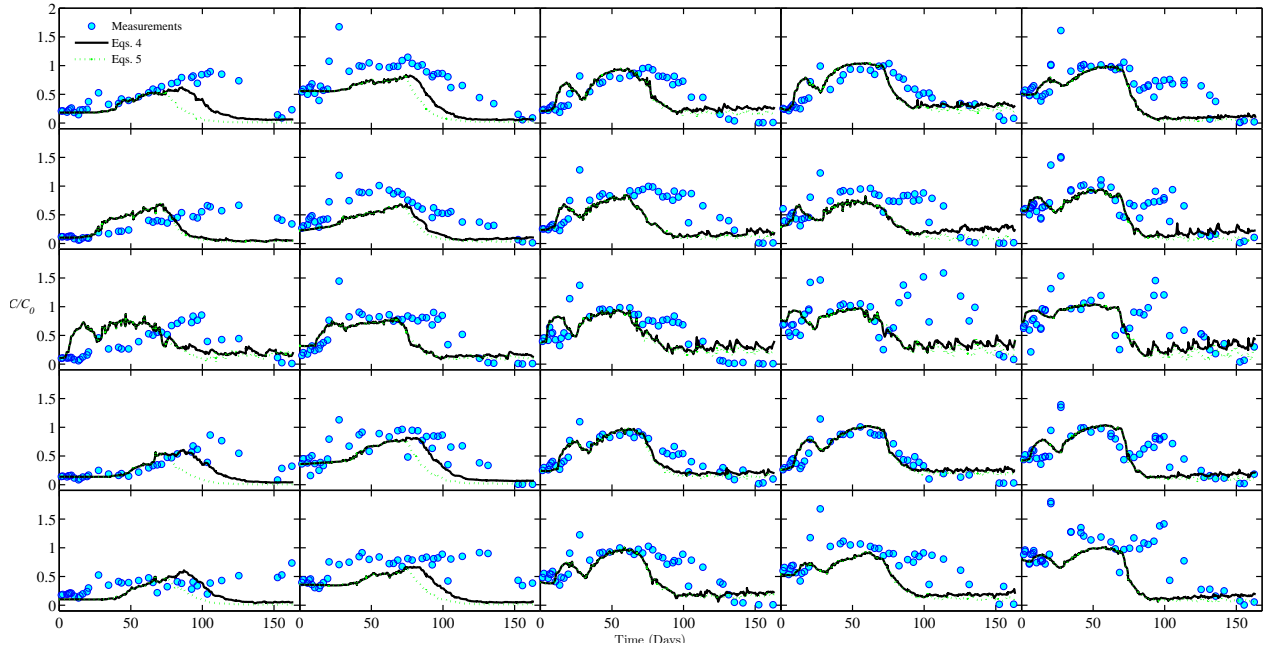
Figure B1. RT3D-simulated breakthrough curves of CT using Eqs.4 and 5. Symbols are the measured concentrations; the black solid lines are RT3D simulations using Eqs.4, and the green dotted lines are simulated results from RT3D model using Eqs. 5. Bold, dashed numbers denote well and sampling depth (ft bgs). Subplots for individual wells are the same locations as in Figures 7 and 8
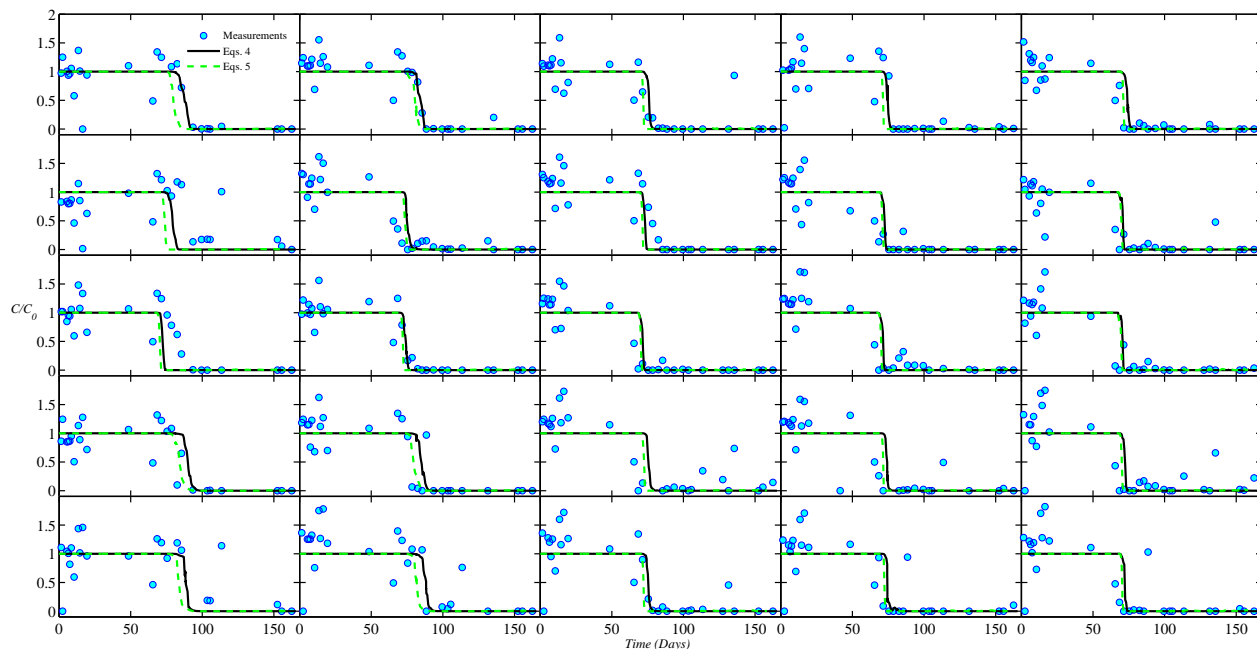
Figure B2. RT3D-simulated breakthrough curves of nitrate using Eqs.4 and 5. Symbols are the measured concentrations; the black solid lines are RT3D simulations using Eqs.4, and the green dashed lines are simulated results from RT3D model using Eqs. 5. Bold, dashed numbers denote well and sampling depth (ft bgs). Subplots for individual wells are the same locations as in Figures 7 and 8
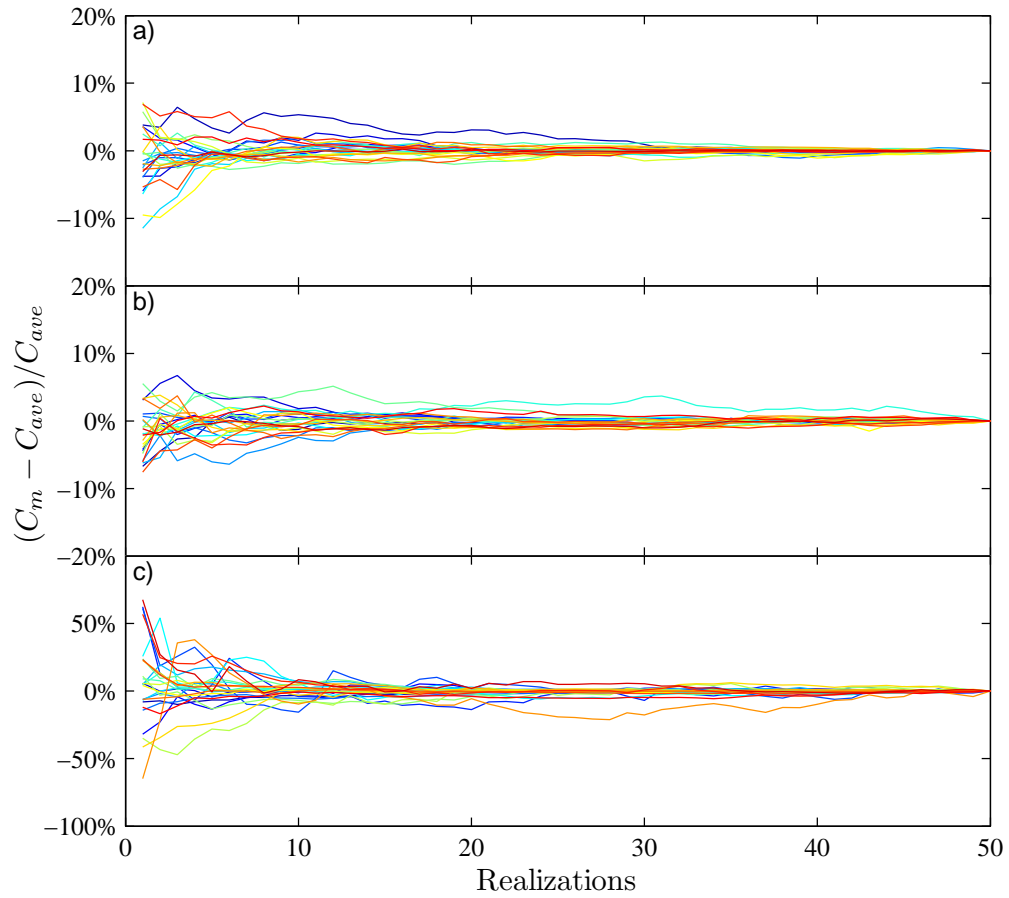
Figure C1. The ratio of the difference between moving average (C_m) and final average (C_{ave}) over final average of nitrate concentrations at 25 well locations at days 30 (a), 72 (b), and 122 (c), which correspond to before, during, and after the injection process, respectively.